acoustics

MDPI

Article

Single-Step Calibration of Remote Microphone Probes Using Bayesian Inference

Riccardo Zamponi [1,2,*] and Olivier Moriaux [2]

[1] Environmental and Applied Fluid Dynamics Department, von Karman Institute for Fluid Dynamics; Waterloosesteenweg 72, B-1640 Sint-Genesius-Rode, Belgium
[2] Wind Energy Section, Flow Physics and Technology Department, Delft University of Technology, Kluyverweg 1, 2629 HS Delft, The Netherlands
* Correspondence: riccardo.zamponi@vki.ac.be

Abstract

The empirical calibration of remote microphone probes, used to acquire unsteady pressure fluctuations in a wide range of fluid-dynamic applications, often introduces spurious resonance into the estimated frequency response, i.e., the transfer function, of the probe over the multiple steps it requires. To prevent this spurious resonance from affecting the unsteady pressure measurements, the transfer functions tend to be manually post-processed. Yet, such a procedure can constitute an additional source of uncertainty that hampers the accuracy of the results. A semi-empirical calibration method based on Bayesian inference was previously developed to tackle this problem: ASSIST (B**A**yesian proce**S**sing of **S**pur**I**ous re**S**onance in calibra**T**ion data). Through this technique, spurious resonance is removed and replaced with a physically correct alternative in a much less operator-reliant manner. However, its application requires a thorough understanding of the model and the related assumptions. This paper provides the knowledge required to apply ASSIST to the calibration of remote microphone probes. It covers the acquisition of the calibration data, the set-up of the method, the analysis of the results, and the iterative tuning of the input parameters to achieve the optimal fit. These steps are demonstrated on an open-source acoustic finite-element method simulation dataset, allowing the analytic line-cavity model to be compared with a 3D model and the impact of the relevant parameters constituting the method to be discussed. This framework is finally used to propose a novel development of the technique that reduces the calibration process of remote microphone probes to one single step, removing the source of the spurious resonance and enabling their in-situ calibration on non-sealing surfaces.

Keywords: microphone calibration; remote microphone probe; bayesian inference; wall-pressure fluctuations

Check for updates

Academic Editors: Mats Åbom and Stéphane Moreau

Received: 8 May 2026
Revised: 15 June 2026
Accepted: 12 July 2026
Published: 16 July 2026

Copyright: © 2026 by the authors. Licensee MDPI, Basel, Switzerland. This article is an open access article distributed under the terms and conditions of the Creative Commons Attribution (CC BY) license.

1. Introduction

Unsteady wall-pressure fluctuations are often acquired to investigate the aerodynamic and aeroacoustic performance of a body immersed in an airflow, e.g., to analyze the generated steady and unsteady forces [1], the pressure distributions on airfoils [2] or rocket nozzles [3], and the turbulent structures within the boundary layer, which can provide valuable information on the noise sources associated with fluid-structure interactions [4].

Microphones are typically used in this context because of their superior frequency response and accuracy. In contrast to being flush-mounted to the wall, a typical strategy is

to mount them remotely from the surface as remote microphone probes (RMPs), i.e., behind a pinhole or a system of tubes and cavities. This arrangement enables the probe to be employed in a wider array of geometries, as the bulky microphone can be positioned away from the surface. The smaller diameter of the pinhole with respect to that of the flush-mounted microphone has two additional benefits. First, the probes can be positioned closer together in an array, improving the correlation-length estimation and, hence, the convection-velocity calculations. Second, the sensing area of the probe results in spatial averaging of high-frequency pressure fluctuations. Models such as that of Corcos [5] can be used to partly correct this effect but rely on several assumptions [6]. Reducing the sensing area mitigates the impact of potential errors introduced by such models.

However, RMPs need to be calibrated to account for the viscous attenuation, reflections, and phase delay of the acquired pressure-fluctuation waves within the system of tubes and cavities. The impact of these effects on the frequency response of the probe is characterized by its transfer function (TF). Using this TF, any acquired unsteady pressure measurements can be corrected for the influence of the RMP geometry [7]. Many analytic methods that model the propagation of pressure fluctuations through the RMP exist [8–14]. Yet, the effective geometrical model parameters can differ from their physical counterparts, e.g., due to manufacturing inaccuracies, end-effects of the tubes, or additional cavity volumes situated between the microphone protective grid and membrane. Any error or uncertainty in these model parameters directly translates into the TF estimate, and any TF error subsequently propagates to the TF-corrected pressure measurements.

Hence, the empirical calibration [15] (p. 70) of RMPs remains the convention. Such methods rely on relating the frequency response of the RMP to that of a flush-mounted reference microphone (ref) when excited by identical pressure fluctuations over the frequency range of interest. This requires a controlled environment in which to position the probes and generate a pressure signal, e.g., a plane-wave tube. As the maximum usable frequency of such a plane-wave tube is inversely proportional to its diameter, the RMP and reference microphone cannot be installed simultaneously. Therefore, two or more calibration steps are generally required, using a calibrator microphone (cal) to relate both steps (1) and (2) together:

$$\mathrm{TF}_{\mathrm{RMP}\to\mathrm{ref}} = \frac{\mathrm{TF}^{(1)}_{\mathrm{cal}\to\mathrm{ref}}}{\mathrm{TF}^{(2)}_{\mathrm{cal}\to\mathrm{RMP}}} = \frac{S^{(1)}_{\mathrm{cal,ref}}}{S^{(1)}_{\mathrm{cal,cal}}} \frac{S^{(2)}_{\mathrm{cal,cal}}}{S^{(2)}_{\mathrm{cal,RMP}}}, \tag{1}$$

$S_{\mathrm{x,y}}$ being the cross power spectral density between the signals x and y.

In Equation (1), it is assumed that the power spectral densities of the calibrator microphone in both steps cancel out, i.e., $S^{(2)}_{\mathrm{cal,cal}}/S^{(1)}_{\mathrm{cal,cal}} = 1$, which means that the pressure field inside the calibrator must be identical, at least up to a multiplicative constant. In general, this is not the case: when the calibrator is placed over the small sensing area of the RMP or that of the large flush-mounted microphone, the wall impedance changes, which results in a difference in the internal pressure field for an identical pressure-fluctuation source [16]. As a consequence, the resonant frequencies linked to the calibrator will slightly shift in frequency and no longer cancel out when combining the TFs. This causes spurious calibrator-induced resonance to appear in the final empirical TF estimate of the RMP. In addition, the conditions to which the RMP is subjected during calibration can differ from those during the measurements, i.e., no grazing flow over the RMP inlet port and possibly a different mean temperature and static pressure. This difference in conditions implies that the TF acquired during calibration differs from the TF of the probe during its measurements, possibly leading to them being corrected by an inaccurate TF [1].

These two families of methods differ in the number of calibration steps they require. The analytic models mentioned above constitute, in principle, a single-step calibration, since the TF follows directly from the probe geometry and the fluid properties without a calibrator or a reference microphone [10]. The infinite-line probe of Englund and Richards [17] is an early realization of this idea. This route has however not replaced empirical calibration because its accuracy is bound to the precision with which the internal geometry and the flow conditions are known. As discussed above, end-effects, manufacturing tolerances, and unmodeled cavity volumes shift the effective parameters away from their nominal values, so the purely analytic TF tends to serve as a first estimate rather than as a calibration. Empirical calibration lifts this reliance on an a priori geometric model, but it is multi-step by necessity: the plane-wave tube prevents the RMP and the reference microphone from being installed at once, and the two sensors present different wall impedance, so they cannot be exposed to the same pressure field at the same time. The calibrator microphone in Equation (1) links the separate steps, and this linking is what admits the spurious resonance described above [16,18]. An accurate single-step calibration that combines the directness of the analytic route with the fidelity of the empirical one has therefore remained unavailable, as the operator accepts either the parameter uncertainty of a purely analytic TF or the calibrator-induced resonance of a multi-step empirical one.

The spurious resonance tends to be manually removed from the TF. Nevertheless, this requires considerable operator expertise to understand which resonance is spurious and how to correct the affected frequency bands with a physically accurate TF [16,19]. This manual intervention is subject to human error and can thus introduce new uncertainties in the TF. More generally, the suppression of spurious resonance can be framed as a signal-processing problem acting on the calibration data alone. The most direct approach is to smooth the empirical TF, for instance with a moving-average filter, but a window wide enough to suppress the spurious resonance also flattens the physical resonant peaks and distorts their phase slopes, since both are narrowband features of comparable shape. The signal-blending of Van de Wyer et al. [16] mitigates this by smoothing only after combining the two source signals, over a limited band and at low strength. More elaborate data-driven techniques decompose wall-pressure signals into their physical constituents, for instance separating the acoustic and turbulent contributions through blind source separation, proper orthogonal decomposition [20], or empirical mode decomposition [21]. All of these rest on the statistical or spectral signature of the data alone, with no physical criterion to assign a given resonance to the probe or to the calibrator, and they therefore remain operator-dependent and can themselves introduce spurious features.

A novel semi-empirical calibration method has recently been proposed to address this problem [22]. The approach, which is referred to as ASSIST (B**A**yesian proce**S**sing of **S**pur**I**ous re**S**onance in calibra**T**ion data), aims to remove spurious resonance in a less operator-reliant, physics-driven manner. An analytic TF model is fitted onto the empirical calibration data using Bayesian inference (BI). In contrast to the filtering and separation techniques discussed above, which rely on the data alone, ASSIST draws on two sources of information at once: the empirical calibration data and an analytic model of the pressure-wave propagation through the probe. This physical model, absent from purely data-driven methods, is what makes the distinction between physical and spurious resonance possible, replacing the affected band with a physics-derived alternative. In doing so, all resonance, attenuation, and phase delay that are physical to the probe are accounted for in the TF while removing resonance that cannot be produced by the considered RMP. Furthermore, the model parameters found in the fitting process can be used with additional corrective models for either the TF [23] or the unsteady pressure measurements [5]. By considering a probable range of parameter values next to the model fit, BI is expected to provide fitting solutions

that are less likely to be pulled towards infeasible solutions due to the presence of spurious resonance in the data compared to simpler fitting methods. BI has been considered for many other problems that augment empirical data with models [24–26], including recent work on Bayesian calibration and uncertainty quantification in acoustics [27,28] and the separation of the acoustic and aerodynamic components of wall-pressure measurements [29].

A validation of ASSIST has already been performed on inviscid acoustic finite-element-method (FEM) simulation data of a plane-wave tube [30], followed by an in-depth investigation using several real-world calibration datasets [22,31]. These previous analyses showed that the semi-empirical method could fit calibration data from a large range of probes, from a simple pinhole configuration to a more complex branching RMP, while removing spurious resonance and replacing the affected frequency bands with a physically correct TF. This approach results in a much smoother TF-corrected wall-pressure spectrum (WPS), identical to what would be achieved within these frequency bands if they were not affected by spurious resonance. The use of BI additionally implies that ASSIST can return the uncertainty bounds of the TF fit.

Yet, whereas the results are much less operator-reliant and hence less prone to introducing errors into the TF with operator intervention, the initial time investment needed for setting up the required code is larger than that for manual post-processing. Moreover, several parameters might need to be tuned iteratively to get the best TF fit, and some basic understanding of the chosen BI algorithm and the analytic frequency response model is required to set up the method. Therefore, the goal of this paper is twofold. On the one hand, it serves as a guide to operating ASSIST and its publicly available Python code [32,33]. The guide outlines the processing of time-series calibration data, the choice of the appropriate parameters for the BI method, and the post-processing of the above-mentioned artificial FEM dataset [30]. This simulated dataset is chosen as the geometry is accurately known, the environment is controlled, and the impact of the chosen model assumptions can be seen. The known geometry is essential here, since it is what allows the parameters recovered by ASSIST to be benchmarked against their ground-truth values, which is not possible with physical probes whose true internal dimensions are uncertain. The removal of spurious resonance from real, viscous calibration data affected by it has already been established on several physical probes in the original study [22] and in the recent work of Zingale et al. [34], while real single-step empirical calibration data are also treated in Section 4. On the other hand, this study aims to present a novel development for ASSIST that allows the calibration procedure of RMPs to be reduced to a single step, making it possible to further overcome the limitations associated with the aforementioned two-step calibration approach and enable in-situ calibrations on non-sealing surfaces.

The remainder of the paper is structured as follows. The chosen analytic model and the general working principles of BI are explained in Section 2. The FEM simulation setup is presented here as well. A detailed guide to setting up the proposed method for the FEM dataset is outlined in Section 3, whereas the discussion of the results is provided in Section 4. Finally, the concluding remarks and several potential future improvements of ASSIST are mentioned in Section 5.

2. Theory and Methods

The semi-empirical calibration approach employed in the study is built upon two theoretical parts that are explained in this section. First, the analytic frequency response model for pneumatic systems is introduced in Section 2.1. Second, the theory of BI is briefly detailed in Section 2.2. The contents and structure of the publicly available Python (version 3.9.12) [32] code used in this study are presented in Section 2.3. Finally, the acoustic simulation setup built to generate the reference calibration data is described in Section 2.4.

2.1. Line-Cavity Model

For the purpose of describing the TF of an RMP, the model of Whitmore [12] (W) is chosen. Similarly to other available analytic models [8–11,13,14], it is based on linearized governing equations for the internal propagation of pressure fluctuations within tubes. The W model discretizes the geometry of the RMP with line-cavity elements, such as in Figure 1. Each line-cavity element has a line with a length L, a constant circular cross-section with a radius R, and a cavity at the end of the line with a volume V_v. This approach assumes that $L \gg R$, the cavity is acoustically compact, and the internal pressure fluctuations remain small enough to result in laminar flow [12,35].

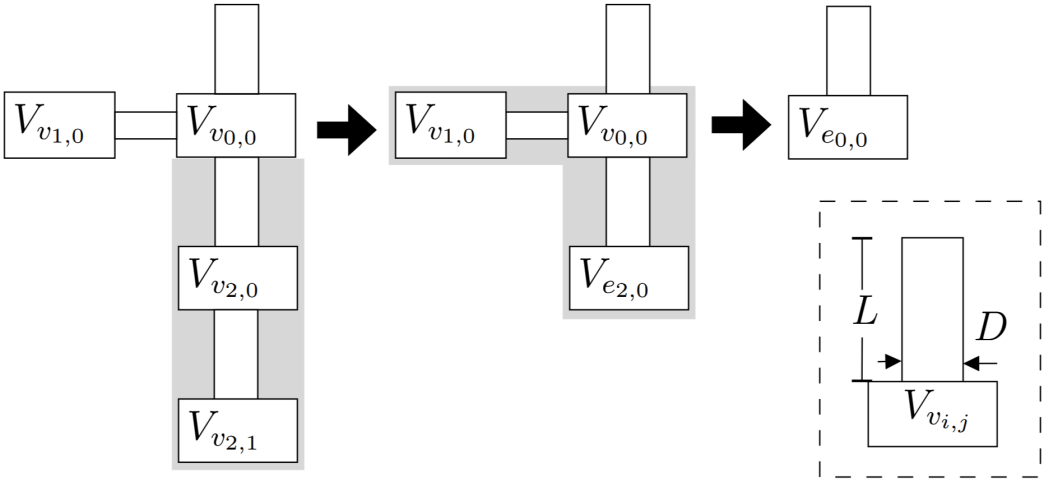


Figure 1. Diagram showing how branching line-cavity geometries are reduced into effective serial ones in the W model. The grey-shaded line-cavities are reduced into the effective volumes in each step.

Compared to the well-known method of Bergh and Tijdeman [10], the W model allows for branching RMP geometries. This is achieved in a similar way to Kirchhoff's laws, i.e., by reducing the impact of any serial or parallel geometry downstream of the considered line-cavity into a complex-valued effective cavity volume V_e. The following equation is used to compute the ratio of the effective volume with respect to the line volume V_t:

$$\left(\frac{V_e}{V_t}\right)_j = \left(\frac{V_v}{V_t}\right)_j \left[1 + \sum_{i=1}^{N} \Phi_{i,j}\right]; \quad \left(\frac{V_e}{V_t}\right)_N = \left(\frac{V_v}{V_t}\right)_N. \tag{2}$$

Here, the subscript i denotes any line-cavity element connected directly downstream of the currently considered element with subscript j. The last downstream line-cavity of a branch of these elements is indicated by subscript N. The last elements in each branch have an equivalent volume equal to their actual cavity volume. An example of how the impact of all downstream elements on element $(i, j) = (0, 0)$ can be modeled with $V_{e_{0,0}}$ is provided in Figure 1. Here, both elements (1, 0) and (2, 1) are the last elements of their branches, i.e., their effective volumes are equal to their cavity volume.

The effective volume considers the complex impedance $\Phi_{i,j}$ of every line-cavity i coupled to the currently considered element j:

$$\Phi_{i,j} = \frac{V_{t_i}}{V_{v_j}} \left(\frac{V_e}{V_t}\right)_i \left(\frac{c_j}{c_i}\right)^2 \frac{\cosh\langle\phi_i L_i\rangle + \sinh\langle\phi_i L_i\rangle / [\phi_i L_i (V_e/V_t)_i]}{\cosh\langle\phi_i L_i\rangle + \sinh\langle\phi_i L_i\rangle \cdot [\phi_i L_i (V_e/V_t)_i]}, \tag{3}$$

where c_j denotes the speed of sound and ϕ_j is the wave propagation factor, as defined by Bergh and Tijdeman [10]:

$$\phi_j L_j = k_{L,j} \sqrt{\frac{J_0\langle\alpha_j\rangle}{J_2\langle\alpha_j\rangle}} \sqrt{\frac{\gamma}{n_j}}. \tag{4}$$

Here, J_k is the Bessel function of the first kind of order k, γ is the ratio of specific heats, and n_j is the polytropic exponent, with P_r being the Prandtl number, defined as

$$n_j = \left[1 + \frac{\gamma - 1}{\gamma} \frac{J_2\langle\alpha_j\sqrt{P_r}\rangle}{J_0\langle\alpha_j\sqrt{P_r}\rangle}\right]^{-1}. \tag{5}$$

Finally, the remaining variables are the normalized model parameters: the reduced frequency $k_{L,j}$, the shear wavenumber α_j, and the cavity-to-tube volume ratio $(V_v/V_t)_j$:

$$k_{L,j} = \frac{\omega L_j}{c_j}; \quad \alpha_j = (-1)^{3/4} R_j \sqrt{\frac{\omega}{\nu_j}}; \quad \left(\frac{V_v}{V_t}\right)_j = \frac{V_{v_j}}{L_j \pi R_j^2}; \quad \frac{V_{t_i}}{V_{v_j}} = \frac{L_i \pi R_i^2}{V_{v_j}}. \tag{6}$$

The last parameter (V_{t_i}/V_{v_j}) is used to couple the connected downstream elements i to the currently considered element j, and it impacts the complex impedance of element i with respect to element j. Here, ω is the angular frequency, and ν_j is the kinematic viscosity.

With the above parameters determined, the TF of each line-cavity section can be computed and multiplied together to form the full TF from one line-cavity section to another:

$$\mathrm{TF}_j = \frac{p'_j}{p'_{j-1}} = \left[\cosh\langle\phi_j L_j\rangle + \frac{V_{e_j}}{V_{t_j}} \phi_j L_j \sinh\langle\phi_j L_j\rangle\right]^{-1}, \tag{7}$$

where p'_j are the pressure fluctuations in the frequency domain in the cavity of element j.

The parameters in Equation (6) make it possible to fit the model to the calibration data.

From the analysis of Figure 2, it can be seen that k_L impacts the line resonant frequencies, which can also be concluded by reformulating the equations for line resonance:

$$f_{\text{open/closed}} = \frac{c}{2L} \cdot n \;\text{ with } n \in \{1, 2, \ldots\} \;\rightarrow\; n\pi = \frac{2\pi f_{\text{open}} L}{c} = k_{L,\text{open}}; \tag{8}$$

$$f_{\text{half-closed}} = \frac{c}{4L} \cdot m \;\text{ with } m \in \{1, 3, \ldots\} \;\rightarrow\; k_{L,\text{half-closed}} = 2m\pi. \tag{9}$$

The strength of visco-thermal effects on the flow within the tube is influenced by α, as noted by Tijdeman [36]. A more viscous flow, i.e., lower $|\alpha|$, decreases the amplitude of the resonance peaks in $|\mathrm{TF}|$, resulting in a shallower resonant phase-shift slope in $\angle\mathrm{TF}$. In addition, all resonant peaks shift to lower frequencies, i.e., lower k_L. The combination of k_L and α determines the viscous attenuation. Hence, for an equal α in Figure 2, the frequency response of different k_L does not perfectly collapse when plotted on a k_L frequency axis. Lastly, V_v/V_t affects the cavity resonant frequency, following the equation for a Helmholtz resonator:

$$f_c = \frac{c}{2\pi} \sqrt{\frac{A}{V_v L}} = \frac{c}{2\pi L} \sqrt{\frac{V_t}{V_v}} \;\rightarrow\; k_{L,c} = \frac{2\pi f_c L}{c} = \left(\frac{V_v}{V_t}\right)^{-1/2}. \tag{10}$$

This Helmholtz estimate approaches the cavity resonant frequency for increasingly inviscid flows.

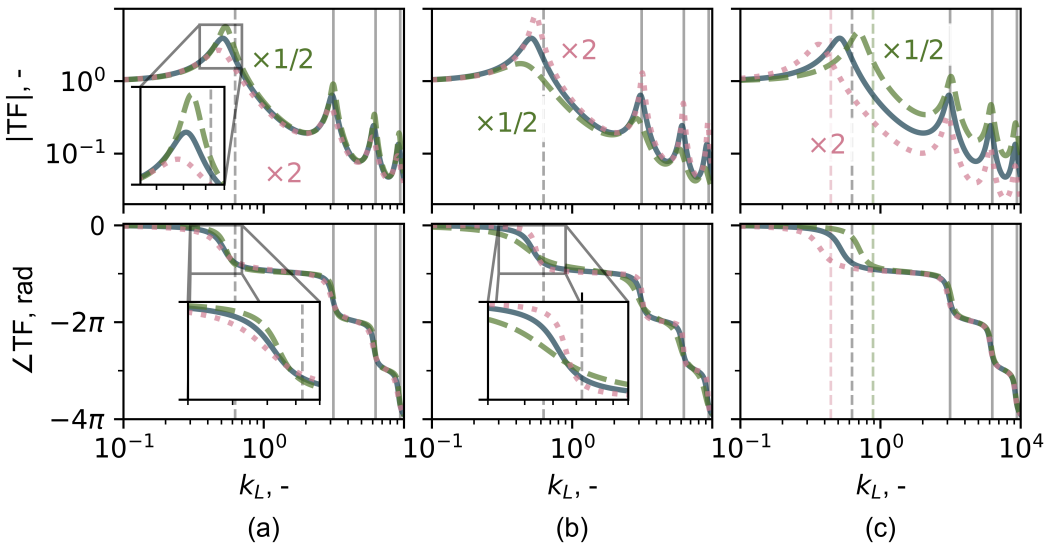


Figure 2. Effect of the normalized W model parameters, see Equation (6), on a single line-cavity element. The vertical lines are resonant frequency estimates: line resonance (Equation (8)) with solid lines and cavity resonance (Equation (10)) with dashed lines. In each panel, the dark solid curve is the baseline, while the pink dotted and green dashed curves show the effect of doubling ('×2') or halving ('×1/2') the corresponding parameter: (**a**) $k_L\ \omega^{-1}$; (**b**) α; (**c**) V_v/V_t. The baseline case is defined by $k_L\ \omega^{-1} = 1.47 \times 10^{-4}$ s, $\alpha\ \omega^{-1/2} = 1.31 \times 10^{-1}$ s$^{1/2}$, and $V_v/V_t = 2.55$, with $\gamma = 1.4$ and $Pr = 0.7$.

2.2. Bayesian Inference

BI provides a natural statistical way to couple a model that reflects the physics of a system to measurements of that system, which makes it ideal for the current fitting problem. Various implementations exist for BI, yet they all feature the following probability density functions (PDFs) at their base: the prior, the likelihood, and the posterior [37]. These PDFs can be found in Bayes' rule [38], which forms the basis of BI, as shown in Figure 3.

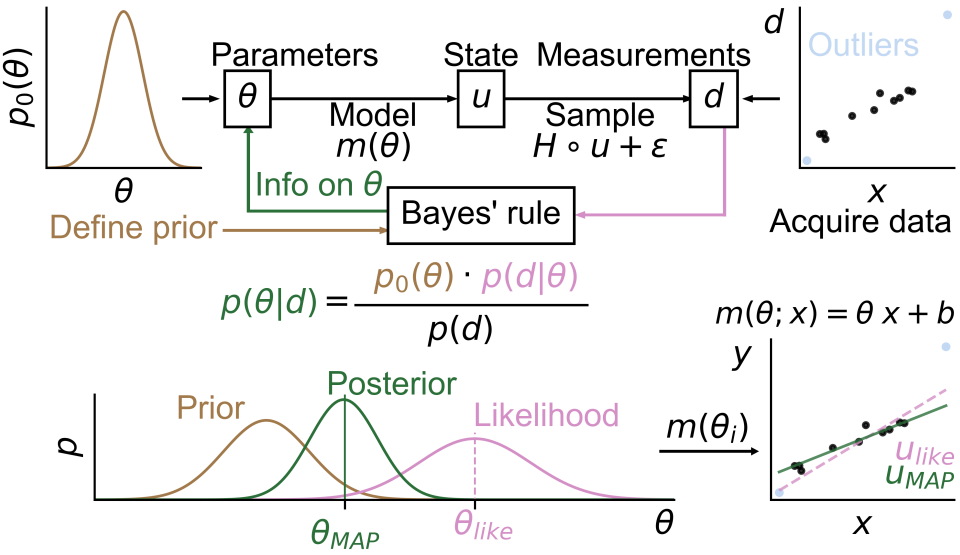


Figure 3. Diagram on the base concept of BI. Bayes' rule is used to infer information on the model parameters θ from two sources of information: (i) the model fit to the data and (ii) the user-defined prior PDF. A most probable system state, without measurement error, is then derived by propagating the parameters with the highest posterior density θ_{MAP} back through the model. Image adapted from Moriaux et al. [22].

The model evidence $p(\boldsymbol{d})$ tends to be ignored for BI since it only scales the posterior and cancels out in most BI implementations. The reason for ignoring this PDF is its

computational cost, as it requires many model evaluations, as can be seen by expanding the model evidence using the law of total probability:

$$p(\boldsymbol{d}) = \int_{-\infty}^{+\infty} p(\boldsymbol{d}|\boldsymbol{\theta})\, p_0(\boldsymbol{\theta})\, \mathrm{d}\boldsymbol{\theta}\,. \tag{11}$$

Hence, the equation for the posterior is often reduced to

$$p(\boldsymbol{\theta}|\boldsymbol{d}) \sim p(\boldsymbol{d}|\boldsymbol{\theta}) \cdot p_0(\boldsymbol{\theta}). \tag{12}$$

This PDF determines the probability of the system having certain parameter values, given the observed measurements, and is simply a combination of the information provided by the prior and the likelihood.

The Bayesian approach considers the following relation between the model parameters and measurement data. Given a fixed set of values for the model parameter vector $\boldsymbol{\theta}$, e.g., geometrical or fluid properties, the frequency response of the RMP is fully defined, e.g., by the model m, and can be considered as the current state $\boldsymbol{u}$ of the system. By calibrating the RMP, one samples this state at several frequencies. The sampling frequencies of the model can be interpolated with those of the data using the observation operator H if they differ. The resulting measurements $\boldsymbol{d}$ also inevitably have some measurement error $\boldsymbol{\varepsilon}$, which can be described by a statistical model. Due to the law of large numbers, it is safe to assume a Gaussian distribution:

$$\boldsymbol{\varepsilon} \sim \mathcal{N}(\boldsymbol{\mu}_\varepsilon, \boldsymbol{R}_\varepsilon). \tag{13}$$

Hence, the measurement error can be split into a systematic ($\boldsymbol{\mu}_\varepsilon$) and a random ($\boldsymbol{R}_\varepsilon$) component. However, with calibration data, the time-domain pressure-fluctuation data of the microphones are transformed into a frequency-domain TF between two such microphones. Any systematic measurement error in pressure fluctuations is located in the TF at $f = 0\,\mathrm{Hz}$. The only way to achieve a systematic error in the TF data is with a scaling error of the pressure fluctuations, e.g., an error in determining the microphone's sensitivity ($\mathrm{mV\,Pa^{-1}}$). Yet, this does not affect the TF phase. Rather, it erroneously scales the entire TF amplitude by a certain amount (see discussion in Section 3.1). And since such errors in microphone sensitivity are case dependent, the systematic error is assumed to be zero, i.e., $\boldsymbol{\mu}_\varepsilon = \boldsymbol{0}$. In addition, it is considered that the measurement errors are unrelated to each other, resulting in a diagonal covariance matrix $\boldsymbol{R}_\varepsilon = \mathrm{diag}(\boldsymbol{\sigma}_{\boldsymbol{d}})$. The specific measurement-error variance is defined by the user, as will be explained in Section 3.3. This error model also sets the robustness of the method to noise. As the TF deviations are taken to be zero-mean and uncorrelated, random noise averages out in the fit, and a clear resonance suffices to recover the probe dimensions even when surrounded by noise. The zero-mean independent Gaussian model is a deliberately neutral choice that avoids biasing the fit with a misspecified noise structure, and it already performs well on real calibration data [22]. It remains a simplification: real measurement chains contain systematic biases, e.g., from microphone-sensitivity estimation, temperature instability, or analogue-to-digital conversion, and errors at neighboring frequencies may be correlated through common noise sources, the calibrator, or the TF estimator. Such non-zero-mean or correlated errors are not captured here and can bias the fit, as for spurious calibrator resonance lying symmetrically around a physical one [22]; these cases are handled by the band-removal of Section 3.4 or by other operator intervention. The method is not tied to this model, however: the user is free to adopt a better-suited error model, treating the parameters or the functional form of its PDF as additional unknowns inferred through a hierarchical MCMC [39], just as the line-cavity model can itself be refined or replaced.

In BI, the first source of information is the data, e.g., the RMP calibration data or the first-order polynomial example with outliers in Figure 3. To achieve a good model fit, a range of $\boldsymbol{\theta}$ can be tested from the parameter space. This information forms the likelihood $p(\boldsymbol{d}|\boldsymbol{\theta})$, which defines how probable it is to observe these measurements given a set of proposed parameter values and some measurement error:

$$p(\boldsymbol{d}|\boldsymbol{\theta}) = \boldsymbol{d} - \boldsymbol{H} \circ m(\boldsymbol{\theta}) = \boldsymbol{\varepsilon} \sim \mathcal{N}(\mathbf{0}, \mathrm{diag}(\boldsymbol{\sigma}_{\boldsymbol{d}})). \tag{14}$$

The parameter vector with the maximum likelihood returns the closest fit to the data, which includes the outliers (see θ_{like} and u_{like} in Figure 3).

The prior $p_0(\boldsymbol{\theta})$ provides the second source of information. It is set by the user based on prior knowledge and assumptions and indicates the probability that a parameter value occurs. Therefore, the posterior will skew the fitting solution proposed by the likelihood towards one with more plausible parameters under the prior (see Figure 3). The most probable parameter values are found at the maximum value of the posterior, i.e., the maximum a posteriori (MAP). The MAP parameters can be fed back through the model to return the most probable system state that resulted in the observed measurements, excluding spurious resonance or any outliers (see θ_{MAP} and u_{MAP} in Figure 3).

For the implementation of BI in this paper, two types of Markov chain Monte Carlo (MCMC) methods are employed. The Metropolis-Hastings (MH) MCMC method is used for most of the presented fitting results, as it more clearly shows the impact of the user-defined proposal distribution. This algorithm is implemented in the publicly available Python code [33]. The second method is the parallel delayed rejection adaptive Metropolis (ParaDRAM) MCMC [40], implemented in the ParaMonte package (version 1.5.1) [41]. This algorithm adapts the proposal distribution to reach a target acceptance rate (AR), which is defined here as 10% to 31% with an adaptive update period of 50 iterations. ParaDRAM is used only where explicitly mentioned in the figure captions. For the associated results, the Markov chain is also resampled multiple times to reduce the correlation between samples, following the standard settings of the ParaMonte package.

MCMC uses random samples from PDFs to sample the posterior, as explained in Section 3.5. Therefore, for the full repeatability of the results, the pseudo-random number generators in the Python code are initialized with a fixed value for the seed of 3751. This ensures that the same Markov chain can be recreated.

2.3. ASSIST Python Code

As mentioned before, the Python code underpinning ASSIST has been made publicly available as an online publicly available repository [33] (version 1.3), which contains the source code, i.e., all the functions to be called within the main scripts of ASSIST and several Jupyter [42] tutorials on all aspects of the semi-empirical calibration approach. The purpose of each script in the repository, as well as the required Python packages and their tested minimum versions, is specified in the included readme file.

Any name of the Python code repository indicated within this paper, i.e., functions, classes, files, or directories, is written in a `monospace` font. The functions mentioned in Section 3 are present in the directory of the source code "`Source`". The ingestion and early processing of the raw calibration data, e.g., computing the TF from the data, are performed with the functions and objects present in `CalibrationMeasurement`. Both TDMS and CSV file formats are supported. This early processing relies on the functions contained within `ProcessingFunctions`. The analytic TF models of Bergh and Tijdeman [10] and Whitmore [12] are implemented as functions and objects in `BerghTijdemanWhitmoreModels`. All functions relevant to BI that are required by ASSIST are stored in `BayesianInferenceFunctions`. Nevertheless, the functions of `scipy.stats`

(version 1.6.0) [43] can be used instead for the prior and likelihood if desired. Finally, the results and calibration data are visualized using the code of `PlottingFunctions`.

2.4. Acoustic FEM Simulation Setup

The internal pressure fluctuations within a plane-wave tube calibrator are simulated using a FEM with an acoustic and vibroacoustic solver, i.e., NASTRAN SOL 108 (Direct Frequency Response), implemented in Siemens Simcenter (version 2304) [44]. The geometry of the plane-wave tube is shown in Figure 4a and is similar to that designed by Van de Wyer et al. [16]. The same acoustic FEM simulation data have previously been used for the validation of ASSIST [30]. This FEM simulation emulates the frequency response of the plane-wave tube used in the empirical calibrations of previous research [16,22]. The empirical calibration data for the single-step approach, presented in Section 4, use the very same calibrator. The data and a Python file to reproduce the TFs considered in this paper are publicly available in the aforementioned code repository [33].

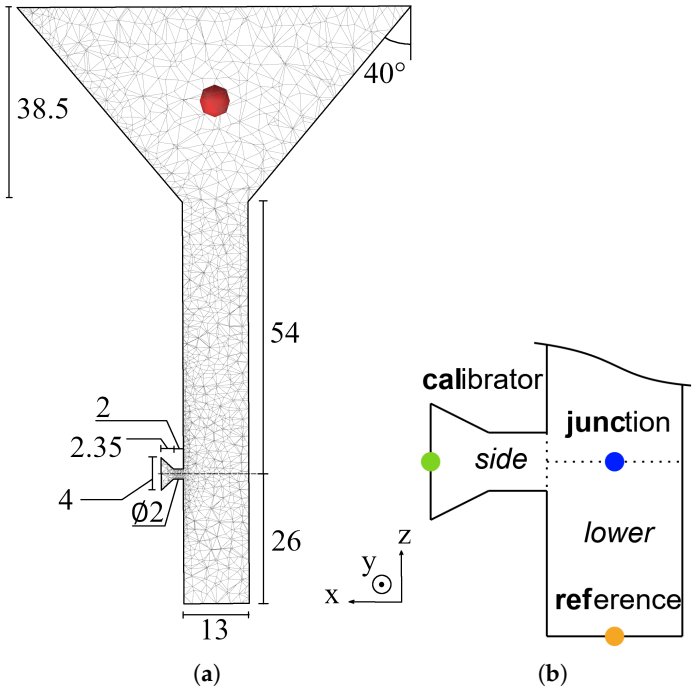


Figure 4. Geometry of the plane-wave tube calibrator used in previous empirical calibrations of experimental campaigns [16,22]. (**a**) Cross-section of the FEM geometry from Moriaux et al. [30], which consists of cylinders and cones. The red dot in the speaker cone indicates the acoustic monopole source. The dimensions are provided in mm and degrees. (**b**) Diagram of the pressure measurement points within the simulation with their names, used to denote the path of the TFs. The italicized names are associated with the line-cavity sections, delimited by dotted lines, and their parameter names. The shown section is the lower part of the geometry depicted in Figure 4a and is not to scale.

A total of 25,422 tetrahedral elements are used to resolve this geometry, with dimensions ranging from 0.7 mm in the *side*-branch of the calibrator to 3.5 mm in the speaker cone of the calibrator. This means that the maximum achievable frequency of this simulation is 16.2 kHz to 9.7 kHz with the largest elements, considering 6 to 10 elements per wavelength, respectively.

The dynamics of the plane-wave calibrator have been simplified by modeling the speaker not as a vibrating surface but as an anechoic boundary, with the pressure fluctuations generated by a monopole source within the speaker cone, indicated by the red dot in Figure 4a. The reason behind this simplification is that the properties of the speaker membrane material need to be determined accurately for the pressure fluctuations to be

correctly generated by the vibrating speaker surface. Instead, this monopole approach simplifies the setup while still generating pressure fluctuations that cover the entire desired frequency range. Additionally, all nodes from which pressure signals are acquired, shown in Figure 4b, are equally affected by the frequency-dependent pressure-fluctuation amplitudes that travel down the main channel of the plane-wave calibrator. Hence, the exact amplitudes of the pressure fluctuations that exit the speaker cone do not matter.

3. ASSIST Setup

Setting up ASSIST with a new dataset can be non-trivial, as there are many choices regarding the data, the model, and the MCMC settings. The following section outlines a straightforward procedure for achieving the best possible results with the proposed method. The first aspect of the semi-empirical calibration approach is the acquisition of calibration data, as detailed in Section 3.1. The setup of the W model for the considered microphone probe examples forms the second aspect of the method and is outlined in Section 3.2. The impact of various choices for the prior PDF is demonstrated in Section 3.3. Pre-processing the calibration data before the fit can, similarly to the prior PDF, be used to fine-tune the TF fit. In Section 3.4, the use of this pre-processing is discussed. Finally, the importance of a properly defined proposal distribution in MCMC is shown in Section 3.5.

3.1. Calibration Data

In general, empirical calibration methods [15,16,18,45] estimate the TF of a RMP by measuring the time-domain pressure fluctuations with microphones over multiple calibration steps, e.g., at the calibrator and reference measurement points of Figure 4b. The design of the plane-wave tube calibrator affects the spurious resonant frequencies and the maximum frequency up to which a usable TF can be estimated, i.e., the cut-off frequency of the plane-wave tube $f_{\text{cut-off}} \approx 0.586\, c/d$ [46], with d being the tube diameter. For example, $d = 13\,\text{mm}$ results in $f_{\text{cut-off}} \approx 15\,\text{kHz}$ (see Figure 4a).

The chosen pressure perturbation signal generated within the calibrator also has an impact on the estimated TF that can be generated from the calibration process. Both frequency-sweep [16] and white-noise signals [7] are popular options. Regardless of the chosen perturbation signal, its amplitude must not clip any microphone in the calibration chain. It is advised to perform a parametric study for the RMP and calibrator combination to determine which calibration signal results in the highest cross-coherence (γ_{ij}^2) between the microphones within the considered frequency range. The impact of these different calibration signals on the TFs should also be observed, e.g., the TF estimate could be inaccurate in a certain frequency band if the perturbation signal does not excite the microphones within that frequency band for long enough or if the measurement time is too short. For the specific measurement campaign performed in the previous study [22], the white-noise signal returned the best results.

The `PressureAcquisition` class offers a very flexible tool for processing time-domain calibration data saved either as TDMS files by a National Instruments LabVIEW virtual instrument or as CSV files, to several frequency-domain metrics such as the power spectral density (PSD), cross-coherence, and TF (see Figure 5). Similarly, the `sensitivity_calculation` function can be used to estimate the microphone sensitivities from calibrations performed using a pistonphone. This is an essential step, as an error in determining the microphone sensitivities results in an erroneous scaling of $|\text{TF}|$, which affects the model fit, e.g., see Figure 5b.

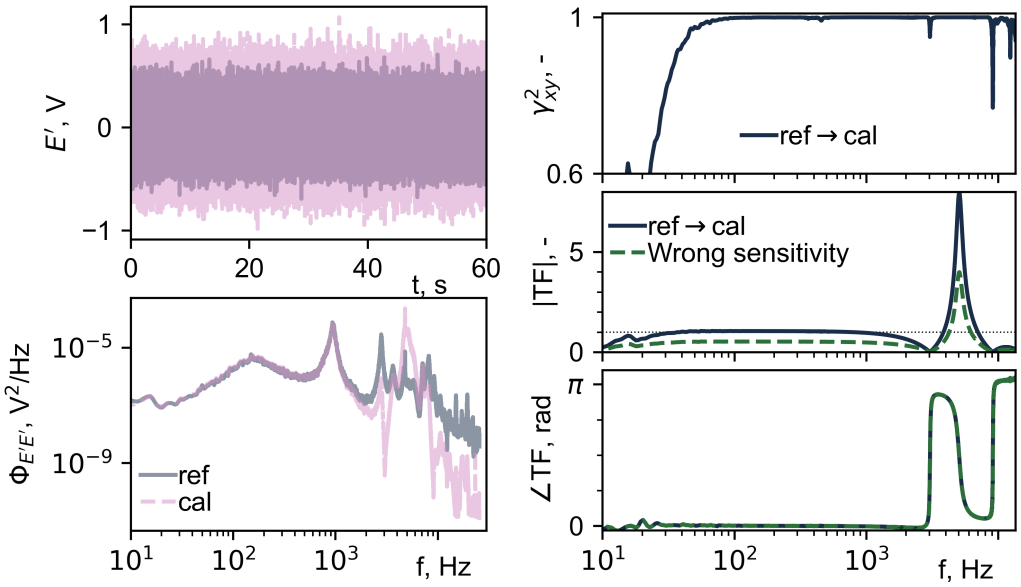


Figure 5. Example processing of the "B&K pinhole" calibration dataset [22] with the `PressureAcquisition` Python class [33]. (**a**) Upper: voltage time-signal acquired during the calibration. Lower: PSD of the voltage signals. (**b**) Upper: cross-coherence between the microphones of the TF. Lower: TF with and without correctly defined microphone sensitivities (exaggerated for demonstration). The dotted line marks the unamplified state.

The FEM data considered for this example are already in the frequency domain. Two TFs are taken as examples and analyzed in this study: (i) a pinhole TF, i.e., from the junction point to the calibrator point, and (ii) a branching RMP TF, i.e., from the reference point to the calibrator point (see Figure 4b). These TFs are shown with the labels '*d*' in Figure 6. For clarity, the term 'RMP' is used to refer to the latter TF case only throughout Section 3, whereas the first case is referred to as 'pinhole'.

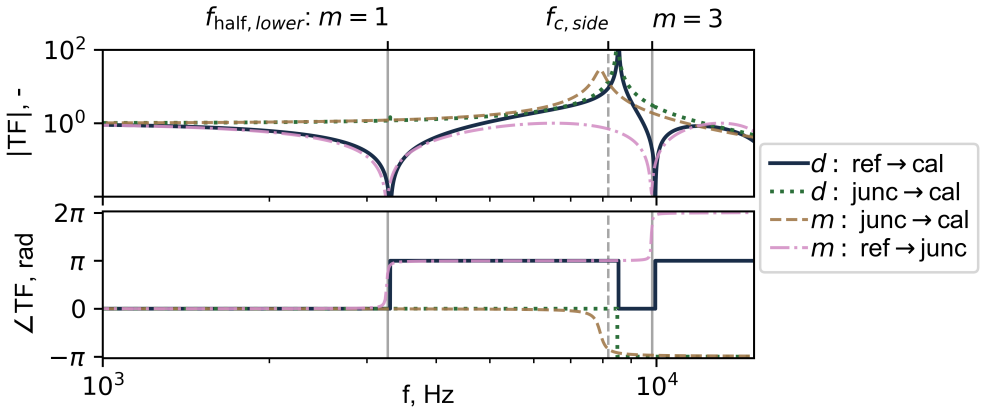


Figure 6. FEM data '*d*' superimposed with the W model TF of the line-cavity elements '*m*'. The vertical lines are resonant frequency estimates: half-closed line resonance (Equation (9)) with solid lines and cavity resonance (Equation (10)) with the dashed line. The naming follows Figure 4b. The *lower* element TF (junc→ref) is inverted to align with the direction of the FEM data TF (ref→junc→cal).

An important design decision to make is how to present the data for BI. Instead of considering the complex-valued TF for the likelihood, the function `frequency_response` is used to compute the real-valued TF amplitude and phase, each with their own σ_d. Real-valued σ_d can be more intuitively set based on the visualized TF. Being able to provide separate values for them allows the operator to prioritize the fit with either |TF| or ∠TF.

Additionally, specific frequency bands of the calibration data can also be band-removed to tune the fit between the model and the data, as will be discussed in Section 3.4.

3.2. Modeling the Microphone Probe

The second aspect of the setup is to define the analytic TF model for both example cases, along with an initial guess of the model parameters. This aspect mostly depends on the prior knowledge of the user regarding the microphone probe geometry and other properties that are relevant to the chosen parameters. This knowledge can be gained from CAD files, simple measurements of the microphone probe dimensions, or updated beliefs gained from previous fitting attempts.

However, depending on the chosen initial guess, the Markov chain might converge to different local optima. A possible solution is to run multiple MCMCs with different initial guesses that cover a range of sufficiently plausible values in the parameter space [39] (p. 283). Such a range would be defined based on the absolute extremes that the parameters can reach or a narrower user-defined parameter range. If the chain converges towards an extreme of either parameter range, a new MCMC run might be needed with updated extremes to better sample in this region of the parameter space. These Markov chains, excluding their burn-in, can then be statistically compared using the double-sided probability of the Kolmogorov-Smirnov (KS) test [47] to determine if the different initial guesses converge to the same PDF mode. This feature is already implemented within the Paramonte DRAM sampler as a multi-chain parallel DRAM, where multiple separate chains are run in parallel [22].

In the current version of ASSIST, the fitting algorithm does not alter the number of line-cavity elements used to discretize the microphone-probe geometry (see Figure 1). The number and connections between line-cavity elements are defined by the user, and ASSIST can only change the parameter values of these elements. Any discontinuities in tube diameter, cavities between tubes, or branches in the probe must be modeled using separate line cavities. These line-cavity elements can be made with `Element` objects and connected to form any microphone-probe shape. Some pre-built functions are also available for pinhole probes and a probe shape similar to the considered branching RMP case, e.g., `whitmore_pinhole` and `whitmore_junction`, respectively.

The TF data of both pinhole and RMP cases, and the W model TFs of the *lower* and *side* line-cavity elements are shown in Figure 6. The initial guess for the parameters of the W model, based on the FEM geometry, already results in a relatively close approximation of the resonant frequencies in the data.

The FEM pinhole case can be modeled using the *side* line-cavity element alone, as is clear from Figures 4b and 6. Hence, the model parameters are $k_{L,side}$, α_{side}, and $(V_v/V_t)_{side}$. For k_L and α, only the real-valued scaling constants are considered for the fitting parameters, i.e., $k_L\ \omega^{-1}$ and $|\alpha|\ \omega^{-1/2}$.

Nevertheless, it is recommended that only a few fitting parameters be selected from the full set of available ones since MCMC methods scale poorly with the number of parameters. In essence, the size of the parameter region in which MCMC needs to sample to find the MAP increases with the size of the parameter vector. As such, other BI implementations should be considered for problems with more than ca. 10 parameters [48]. By using the initial guess for the geometry of the microphone probe, the resonant frequencies of the geometry can be estimated through either the W model or the resonance equations (Equations (8)–(10)). Overlaying these models and resonant frequencies with the data, such as in Figure 6, can indicate the source of the resonance, i.e., which line-cavity element induces the resonant phenomenon and whether it is line resonance or cavity resonance.

For the pinhole TF data, the only resonant frequency is situated near 8.5 kHz and is approximately equal to the Helmholtz resonance of the *side*-branch line-cavity element. To correctly fit this resonance with the model, V_v/V_t is needed to match the resonant frequency, and α is needed to match its attenuation. Therefore, $k_{L,side}$ is dropped from the fitting parameters.

For the RMP case, the TF can be modeled using three elements, which are shown in Figure 4b. The *upper* element has its inlet at the top of the calibrator main channel, i.e., at the end of the conical cavity that houses the speaker, and it ends at the junction point. Hence, the speaker cone is ignored in the W model geometry. The remaining two elements are connected downstream of the *upper* one: the *side* branch and the *lower* section of the calibrator main channel. The latter has a small non-zero cavity volume, as any branch termination of a microphone probe with a zero cavity volume can cause problems for the complex impedance of upstream elements (see Equation (3)).

However, any pressure fluctuation that travels down the *upper* element and reaches the junction point affects both connected line-cavity elements equally. Hence, it can be reasoned that any change in the TF of elements above the junction point has no impact on the RMP TF. The RMP TF can thus be expressed, following the naming in Figure 4b, by:

$$\mathrm{TF}_{\mathrm{ref}\to\mathrm{cal}} = \frac{\mathrm{TF}_{upper}\mathrm{TF}_{side}}{\mathrm{TF}_{upper}\mathrm{TF}_{lower}} = \frac{\mathrm{TF}_{side}}{\mathrm{TF}_{lower}} = \frac{\mathrm{TF}_{\mathrm{junction}\to\mathrm{cal}}}{\mathrm{TF}_{\mathrm{junction}\to\mathrm{ref}}}. \tag{15}$$

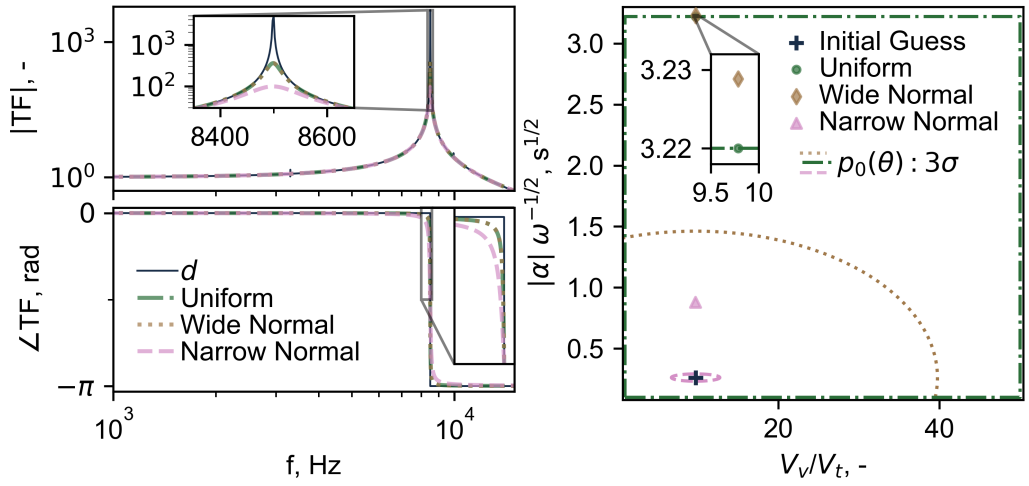
The same conclusion could also be reached by observing Figure 6. The branching RMP TF can be produced from the *side*-branch and *lower* line-cavity elements alone.

Consequently, only model parameters linked to the *side*-branch and *lower* elements must be considered. This results in a preliminary selection of 6 parameters, which all impact the RMP TF: the k_L, α, and V_v/V_t associated with both line-cavity sections. Figure 6 can be used to further reduce the number of fitting parameters. The *side*-branch element only features cavity resonance within the considered frequency range, eliminating the need for $k_{L,side}$. Similarly, the *lower* element only produces half-closed line resonance, removing $(V_v/V_t)_{lower}$ from the fitting parameter selection. Hence, the main parameters affecting the RMP TF are $k_{L,lower}$, $(V_v/V_t)_{side}$, α_{lower}, and α_{side}. Only the first two will be considered, as the main purpose of this example is to fit the resonant frequencies, not their exact amplitude or phase shift slope, and because this choice results in a clearer visualization of the posterior PDF as a single contour plot. With the RMP case using k_L and V_v/V_t as parameters, and with the pinhole case using α and V_v/V_t, the behavior of all three main geometric model parameters as fitting parameters can be observed in this guide.

With the callable function for the model of both cases finalized, the function for the likelihood is complete. Examples of such code are publicly available in the online code repository [33]. However, the MCMC code requires a callable function for the posterior PDF that can be computed at each new proposed parameter sample. The final step needed to form the posterior is to define a prior PDF.

3.3. Prior PDF

Any type of prior PDF can be provided by the user. This PDF should reflect the operator's knowledge about the probability of the system possessing a certain parameter value. Two examples are provided: (i) a uniform distribution spanning a range of parameter values that are deemed possible, and (ii) a multivariate Gaussian centered on the initial guess of parameter values. The impact of different priors on this pinhole case is shown in Figure 7.



(**a**) (**b**)

Figure 7. Pinhole FEM TF fitting results with three different priors. The defined measurement errors are: $\sigma_{d,|\mathrm{TF}|} = 50$ and $\sigma_{d,\angle\mathrm{TF}} = 0.1$ rad. (**a**) TF of the various fitting solutions. (**b**) MAP of the various fitting solutions. The bounds of the uniform prior and the 3σ bounds of the normal priors are indicated with dashed lines of the same color as the MAP markers.

The uniform prior PDF is the least informative, as it simply sets the allowed extremes (see Figure 7b). With this prior, the posterior reduces to the likelihood within the allowed bounds, so the MAP coincides with the maximum-likelihood estimate. Since the likelihood of Equation (14) is Gaussian, maximizing it is equivalent to minimizing $|\boldsymbol{d} - \boldsymbol{H} \circ m(\boldsymbol{\theta})|^2$, i.e., the uniform-prior fit is a bounded least-squares fit of the model to the calibration data [37]. The comparison between priors in Figure 7 therefore already includes a least-squares fit as its uniform-prior case. Due to the large mismatch in the model fit '$\boldsymbol{d} - m(\boldsymbol{\theta})$' around the resonant frequency (see Figure 7a), the likelihood attempts to continuously increase $|\alpha|$. This large mismatch in $|\alpha|$ will be further discussed in Section 4.

The normal prior PDF provides more information to the posterior. The prior mean defines the model parameters that the user deems most probable, and the covariance matrix of the prior reflects the uncertainty of the initial value for each parameter. This covariance matrix has an effect similar to the bounds of the uniform prior. A larger prior variance on a given parameter means it will be allowed to deviate further from the initial value to achieve a closer fit. This is shown with the two normal priors in Figure 7b.

For example, the exact cavity volume of the probe might depend on the mounting of the microphone within the cavity that houses it and the additional volume between its protective grid and membrane. Additionally, since line-cavity models assume a compact cavity, where all inertia of the flow occurs within the tube, a conical cavity might feature an increased effective line length and a decreased cavity volume with respect to their geometrical counterpart. Regardless, it is recommended to permit a larger prior variance on cavity volumes.

It is important to note that the prior variances and σ_d have a combined effect on the model fit. Smaller σ_d values mean that the model fit is allowed to deviate less from the data, more readily changing the model parameters from their initial guess. Inversely, a smaller prior PDF covariance will restrict the deviation of parameter values from their initial values more, possibly resulting in a model fit that is less close to the data. A closed-form equation for the posterior exists for linear models with a Gaussian prior and likelihood [49], and even for non-linear models, this combined effect of variances can be seen in Figure 7b. While the likelihood remains the same, the different covariances of the Gaussian priors allow the MAP parameters to deviate more or less from the initial guess. So, while the prior

covariance matrix and measurement-error variances can be defined based on repeated measurements, they can also be assumed to be simple tuning parameters for the fit. They reflect the relative uncertainty linked to the data and the probable range of parameter values. The exact values for the variances influence the credible regions of the posterior PDF and should thus be considered when using these credible regions for the uncertainty quantification of this method. The sensitivity of the posterior and its credible regions to the chosen prior or measurement error can be evaluated using a Hierarchical MCMC [39]. Here, the prior PDF parameters or σ_d are defined as hyperparameters [22], which also form a part of the MCMC parameter vector. In many cases, defining a prior and σ_d that result in the desired model fit is an iterative process, and they are tuned based on the results of previous runs. For the pinhole probe example, a bad prior may cause the MCMC not to converge due to the continuous increase in $|\alpha|$ (see Figure 7).

Finally, observing the θ_{MAP} of both normal prior examples in Figure 7b, their values fall outside of the 3σ credible region of the prior. In other words, these parameter values have less than 1% chance of occurring according to the prior knowledge of the operator. This may indicate one of the following problems. (i) The operator's knowledge of the parameters, summarized in the prior, does not properly reflect the range of parameter values that the system is likely to have. (ii) The model does not properly reflect the physics that have resulted in the observed data; i.e., the correct parameter values result in a model TF that is completely different from the calibration data. As the exact FEM geometry is known, the mismatch in the model frequency response and calibration data will be further discussed in Section 3.4.

3.4. Pre-Processing the Calibration Data

The previous analysis showed a problematic aspect of the pinhole case: the posterior of this case strongly depends on the chosen prior (see Figure 7b). Depending on the prior, the MCMC might not even converge. The source of this sensitivity is the aforementioned mismatch in peak resonant |TF| and the resonant phase shift slope, caused by the W model being viscous while the FEM simulation is inviscid. Hence, the likelihood will push the W model to emulate the inviscid behavior by perpetually evolving $|\alpha|$ towards larger values.

ASSIST relies on having large enough frequency bands of correct TF data to fit, such that the frequency bands affected by errors are mostly ignored and replaced by the correct TF. The prior partly aids in this task by keeping the model parameters in a physically reasonable range. Yet, sometimes, if the error in the data results in too large a deviation from the model, the fit may prioritize the frequency bands containing the errors to the detriment of the fit within the frequency bands with correct TF data. Two examples of erroneous frequency bands can often be found. First, for all empirical calibration, the experimentally obtained TF data will no longer reflect the frequency response of the probe below or beyond certain frequencies where the calibrator provides an accurate calibration environment, e.g., above the calibrator cut-off frequency (see Section 3.1) or the frequency limits imposed by the microphones. Second, similarly to inviscid resonance in the pinhole case, spurious resonance can be problematic to the fit when (i) the magnitude of the mismatch to the true TF is too large, e.g., Figure 7a, or (ii) most of the acquired frequency band of the TF data is affected by spurious resonance. Hence, besides tuning the prior, the data can be pre-processed before fitting the model: specific frequency bands can be band-removed using the `mask_f_data` function.

With empirical calibration data, the cross-coherence between the different microphone signals used for the TF can serve as a good indicator of the quality of the data at each frequency, often dropping suddenly in correspondence with calibrator-induced spurious resonance, e.g., at 3.3 kHz and 10 kHz in Figure 5b. Therefore, cross-coherence between

the calibration steps can be consulted when choosing which frequencies to band-pass. It is important to stress that resonance should only be removed after careful analysis of its source to avoid removing resonance that is physical to the probe.

In the case of the FEM pinhole, one could deem the inviscid resonance not to be physical to the probe since it does not match the viscous W model. Hence, the TF from 8.4 kHz to 8.6 kHz is band-removed to avoid the negative impact of the inviscid resonance on the convergence of the Markov chain and the sensitivity of the posterior. The method will still be able to fit the resonance in the TF using the remaining increase and decrease of |TF| centered around the resonant frequency, but the fit will no longer be pulled to match the extremely large resonance |TF| peak value (see the inset plot in Figures 7a and 8).

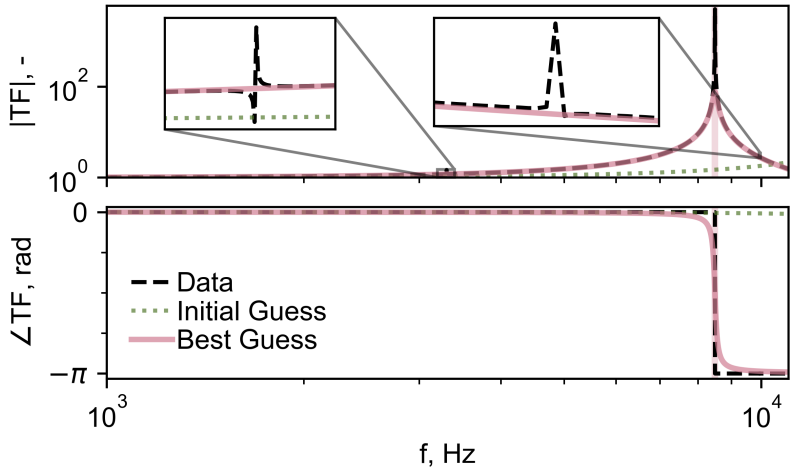


Figure 8. TF fit, using ParaDRAM, of the band-removed pinhole FEM simulations data, $TF_{junction \to cal}$. The red-tinted region from 8.4 kHz to 8.6 kHz is band-removed.

3.5. MCMC Proposal Distribution

For non-linear models, such as the W model, the existence of a closed-form equation for the posterior is not guaranteed. Instead, MCMC estimates the posterior by randomly sampling its PDF based on the value of the posterior in the proposed sample and in the previous sample [50]. Using the MCMC samples, the kernel density estimate (KDE) [51] approximates the posterior.

Various MCMC algorithms evolve the Markov chain by proposing a new sample parameter vector at each iteration i. The MH MCMC algorithm, which shares some similarities with DRAM, is explained here. This proposed parameter vector $\boldsymbol{\theta}_p$ is chosen by taking a random sample $\boldsymbol{g}_i$ from the multi-variate Gaussian proposal distribution, which is centered on the last sample accepted into the chain $\boldsymbol{\theta}_{i-1}$:

$$\boldsymbol{\theta}_p = \boldsymbol{\theta}_{i-1} + \boldsymbol{g}_i \text{ with } \boldsymbol{g}_i \sim \mathcal{N}(\mathbf{0}, \boldsymbol{P}) \,. \tag{16}$$

However, for the KDE to provide a usable estimate of the posterior PDF, the density of the samples should be related to the local probability density of the posterior, e.g., Figure 9b. Equation (16) alone results in a random walk of samples that is unrelated to the posterior. To tackle this problem, the correct sample distribution is ensured by using a criterion based on the ratio of the posterior value in the proposed sample to the posterior value in the last accepted sample:

$$\text{if } \; \Pi = \frac{p(\boldsymbol{\theta}_p|\boldsymbol{d})}{p(\boldsymbol{\theta}_{i-1}|\boldsymbol{d})} > y_i \sim \mathcal{U}(0,1) : \; \boldsymbol{\theta}_i = \boldsymbol{\theta}_p; \qquad \text{else} : \; \boldsymbol{\theta}_i = \boldsymbol{\theta}_{i-1} \,. \tag{17}$$

In Equation (17), the ratio of the posteriors Π is compared with a sample from a uniform distribution y_i ranging between 0 and 1. The result is that any proposed sample with a higher value for the posterior ($\Pi > 1$) is guaranteed to be accepted into the Markov chain, allowing the chain to evolve towards regions of high probability. Nevertheless, proposed samples with a lower value for the posterior still have a non-zero chance of being accepted, as y_i can take any value between 0 and 1.

Starting from the initial guess, it is likely that the sampler will require several samples to converge to a region of high posterior probability around the MAP, ideally in as few steps as possible (see Figure 9b). A large covariance $\boldsymbol{P}$ for the proposal distribution increases the step size between proposed parameter-vector samples, following Equation (16). These burn-in samples, which are required to reach the high-probability region of the posterior, are not distributed in a manner that is representative of the posterior and, therefore, are not usable for estimating the posterior PDF (see Figure 10c). Plots such as the one in Figure 9a can be used to determine which samples must be removed from the chain before computing the KDE. For example, the distribution of the remaining samples in the inset plot of Figure 9b is representative of the posterior.

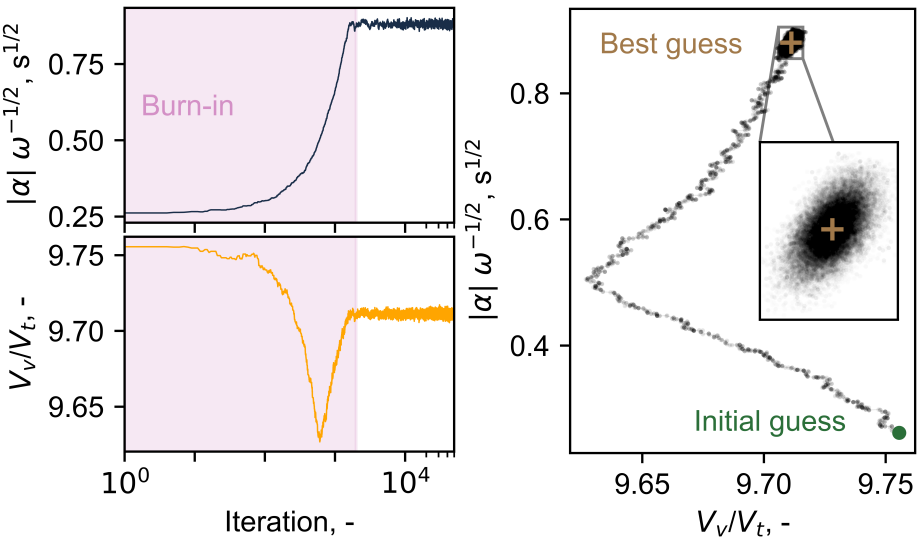
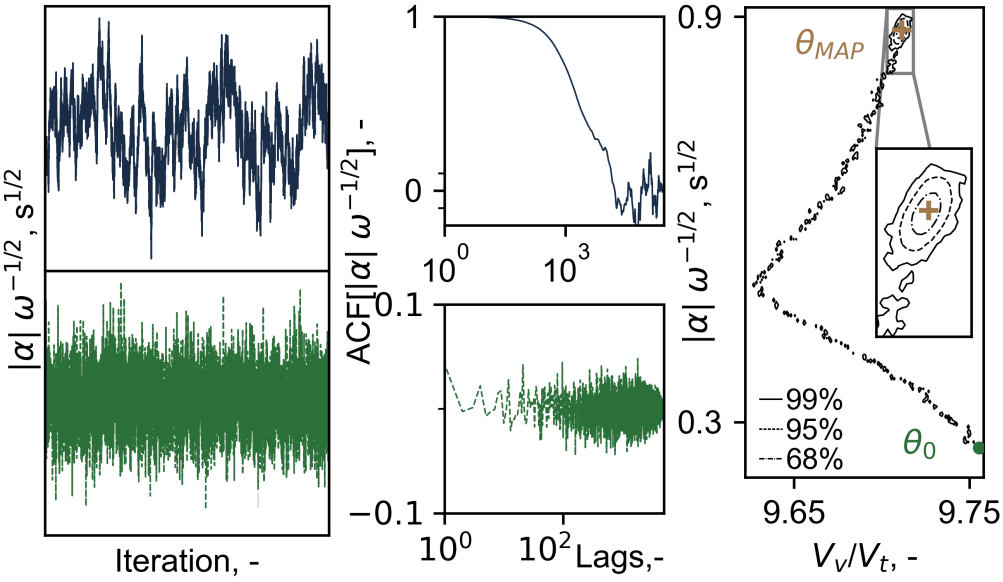


Figure 9. Parameter vector chain of the MCMC of the pinhole FEM case with the 'narrow normal' prior (see Figure 7). (**a**) Per-iteration convergence of the parameter values. (**b**) Convergence of the chain shown in the parameter space.

A smaller step size is likely to result in Π closer to unity. Compared to that, a large step size is more likely to land within a region with a lower posterior than the current sample, hence a smaller Π. Thus, a smaller step size of the proposal distribution will have a lower percentage of rejected samples, which is desirable from a computational cost perspective. Yet, a small step size also means that the parameter values of each sample are more strongly correlated with the parameter values of the previous samples. This correlation is not representative of random samples of the posterior PDF but is linked to the proposal distribution. Hence, using these samples to estimate the PDF might not return an accurate representation of the posterior, and samples with a strong correlation should be sub-sampled. In short, whereas a small step size between samples increases the AR, it also increases the correlation between the samples.



(**a**) (**b**) (**c**)

Figure 10. Examples of the impact of the defined proposal distributions and burn-in. (**a**) Comparison of the MCMC samples with a high AR of 95% (top row) and a low AR of 24% (bottom row). Burn-in samples are removed and the low AR case is sub-sampled. (**b**) Comparison of the auto-correlation function (ACF) for an AR of 95% (top row) and an AR of 24% (bottom row). (**c**) KDE of the highest posterior density credible regions of the 'narrow normal' prior example without removing the burn-in samples (see Figure 9).

In view of the above, the proposal distribution covariance matrix should be tuned to achieve a good trade-off between the number of accepted samples and the correlation between them. This trade-off is found at a sample AR of approximately 30% for the samples after burn-in [48]. Gelman et al. [39] (p. 296) suggest a slightly different target AR of 44% for 1-D problems and 23% for higher dimensional problems, i.e., above approximately 5-D. Both sources also advise shaping the proposal distribution to match that of the posterior, albeit scaled to achieve the target AR.

As an example, the link between AR and the correlation of the Markov chain samples is demonstrated in Figure 10. Regardless of the proposal distribution and AR, the underlying posterior remains the same. Therefore, the Markov chain will randomly sample within a similar parameter value range, i.e., similar extremes (see Figure 10a). However, for a small step size, it will take many more iterations to evolve from one extreme of this high probability parameter range to the other. This implies that the parameters in each iteration are closer in value to those of the surrounding iterations. The result is that the chain exhibits a periodicity similar to the 95% AR case in Figure 10a. In comparison, the large step size of the low-AR case results in a Markov chain that can jump from one extreme of the parameter space to the other and randomly pick any value in between. Another way of observing this is with the auto-correlation function (ACF) of the sample parameter values, computed with ParaMonte [41], which simply quantifies the correlation between pairs of samples of the Markov chain that are separated from each other by a certain amount of sampling iteration 'lags'. For the high AR case, the ACF for $|\alpha|$ remains large up to a very high number of 'lags' (see Figure 10b). In other words, samples up to 10^4 iterations away from another sample are correlated with it. In comparison, the low AR case has very low values for the ACF, even for samples that are situated close to one another. Naturally, when running the first MCMC attempt for a new case, the AR after burn-in is likely not to represent the desired value. While tuning the proposal distribution, the AR may overshoot that

desired value for the first few MCMC runs. Hence, tuning the proposal distribution can require several MCMC runs. Apart from the proposal distribution, enough samples in this high-probability posterior region are needed for the KDE to converge to an accurate estimate of the posterior PDF.

DRAM is capable of adapting the proposal distribution every couple of iterations [40]. As such, ParaDRAM can start with larger steps during burn-in and shrink the step size in a posterior region with high probability. In addition, ParaMonte will sub-sample the final MCMC chain to reduce the correlation between samples [41]. Still, understanding the principles of MH MCMC can be beneficial, and the publicly available code has the MH MCMC method implemented in the `mcmc_update` function.

The KDE associated with the band-removed pinhole case with ParaDRAM is presented in Figure 11. The contours visualized from the KDE are the highest posterior density regions associated with the credible regions of 68%, 95% and 99%. These are the credible region contours with the largest mean value for the PDF. In other words, these are the narrowest range of parameters that contains the defined credible region. For example, the integrated space under a Gaussian PDF that defines the credible region could be achieved with the parameter range of the tails of the PDF or the parameter range that contains its peak.

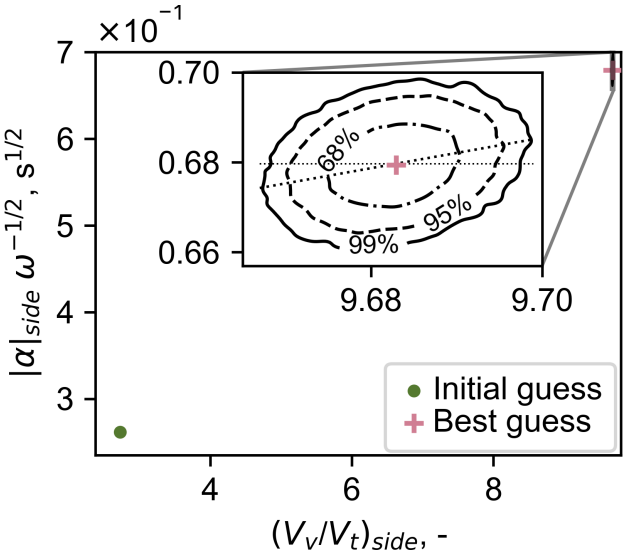
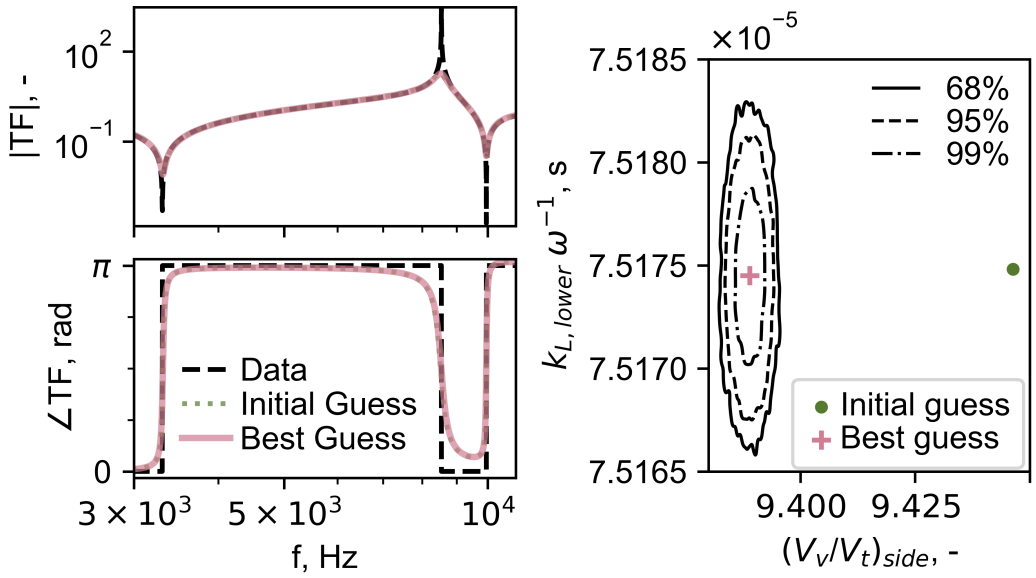


Figure 11. KDE of the TF fit of pinhole FEM simulations data, $TF_{junction \rightarrow cal}$. TF fit, using ParaDRAM, shown in Figure 8.

The KDE contours of the pinhole indicate a positive correlation between the model parameters $|\alpha|_{side}$ and $(V_v/V_t)_{side}$, as can be seen from the positive angle of the elliptical KDE contour axes to the coordinate axes (see the dotted lines in the inset figure of Figure 11). The correlation between these parameters has also been observed and discussed in detail in previous research [22]. Since a higher $|\alpha|$ increases the resonant frequencies, V_v/V_t or k_L need to increase for the model to still retain the same resonant frequency as that present in the data (see Figure 2).

4. Results and Discussion

The general procedure to set up ASSIST for microphone calibration data has been detailed in the previous sections. The results of processing both TF cases with ASSIST are presented in the following section. The application of this method to the RMP case results in Figure 12.



(**a**) (**b**)

Figure 12. Fitting results for the RMP FEM case using ParaDRAM. (**a**) $TF_{ref \to cal}$ fit. (**b**) KDE of the MCMC TF fit.

For both pinhole and RMP cases, the TF returned by ASSIST contains all resonant frequencies present in the data, as shown in Figures 8 and 12a, respectively. This would not have been the case if the model assumptions were invalid for the calibration data [30] or if the probe geometry was not properly represented by the user-defined line-cavity topology [22].

Similarly to the 8.5 kHz *side*-branch resonance, the destructive line resonance at 3.3 kHz and 10 kHz in the RMP TF does not reach as low a value for |TF| nor as steep a phase shift slope due to the difference in $|\alpha|_{lower}$ between the FEM and W model (see Figure 12a). However, for the RMP case, $|\alpha|$ is not part of the fitting parameters; therefore, the mismatch in viscosity between the data and the model does not pose an issue for the TF fit.

These line-resonant frequencies in the RMP data are also present in the pinhole TF as spurious resonance at 3.3 kHz and 10 kHz, which is shown in the inset plots of Figure 8. For 1-D models, such as the W model, the *side*-branch line-cavity element is connected to the *upper* line-cavity element at the junction point (see Figure 4). The pressure fluctuations in the junction point are imposed over the entire cross-section of the *side*-branch line-cavity element as inlet conditions. Hence, the entire element is equally affected by the line resonance, just as the junction point is. As a TF is a comparison between the signals in two points, and all points in the *side* branch are equally affected by the line resonance, the resonance does not appear in the W model of the pinhole TF.

In comparison, for the 3D acoustic FEM simulation, the pressure fluctuations imposed at the inlet of the *side* branch are not only those at the junction point, where the line-resonant node is located, but also those in the plane-wave tube over the entire 'sensing area' of the *side* branch (with a diameter of 2 mm). Therefore, a remnant of the line resonance is present in the FEM simulation pressure fluctuations in the calibrator point. This might be considered an impact of the 1-D flow assumption of the W model. However, such small features in the TF are likely to be dissipated for real viscous calibration data, and the semi-empirical method successfully removes and replaces the TF in frequency bands affected by spurious resonance. Furthermore, although a correlation between $|\alpha|$ and the other W model parameters exists in Figure 11, the RMP case shows that no correlation exists between k_L and V_v/V_t, as shown in Figure 12b. This is deduced from the elliptical

KDE contours being upright. In other words, the principal axes of the elliptical contours are aligned with the parameter axes. The lack of correlation is due to both parameters having no effect on the resonant frequency of each other; i.e., V_v/V_t has no impact on the line-resonance, and vice versa for k_L. However, this lack of correlation is by no means universal. For viscous TFs, nearby resonance may cause their resonant frequencies to shift toward one another.

Another point of interest is how close the MAP parameter values are to the 'true' parameters of the pressure-measurement probe. The W model assumptions [12,36] imply that the physics of the model are not an exact representation of the real system. As such, the TF of the real and model systems may differ, even when the same parameter values are considered. For the goal of removing spurious resonance from the calibration data, this is of little relevance, as a matching TF can be found with slightly different parameter values. However, any use of the resulting MAP parameters would suffer from this problem, e.g., inserting the MAP parameters into corrective models for either the TF or pressure measurements. For example, using $|\alpha|$ of the pinhole as a fitting parameter, an estimate of the true system radius of the pinhole is provided as the MAP. This quantity can be used in the model of Corcos [5] to correct any wall-pressure spectra acquired with the microphone for spatial averaging of the unsteady pressure fluctuations over the sensing area of the probe. Similarly, the MAP dimensions of the probe and the resulting TF fit can be used to apply a correction for the effect of grazing flow over the microphone using the model of Tijdeman and Bergh [23]. However, the accuracy of these corrections depends on how well the MAP-parameter values represent the real-parameter values.

The results of the W model are, to some extent, similar to those of the model of Bergh and Tijdeman [10]. The latter study mentions that similar TFs are achieved between the model and data for tube radii that are 2 % to 5 % smaller than the mean true values. For the FEM data, the MAP parameters are expected to differ from the true values due to the aforementioned correlation between parameters and the difference between the inviscid data and the viscous W model. No comment can be made about the difference in $|\alpha|_{side}$ between both FEM geometry and the set of MAP parameters, as the inviscid simulation does not have a value for ν. As shown in Table 1, the other two MAP parameters differ significantly from their counterparts in the FEM geometry.

Table 1. Difference between the MCMC parameter MAP values and the FEM geometry.

Parameter	$k_{L,lower}\ \omega^{-1}$, s	$(V_v/V_t)_{side}$, -
MAP	7.52×10^{-5}	9.39 (RMP), 9.68 (pinhole)
FEM	7.64×10^{-5}	2.74

For real-life calibration data, the initial guess of the parameters appears to lie closer to the MAP parameters [22]. Still, it proves difficult to determine the 'true' model parameters of the physical microphone probes to validate the accuracy of the MAP parameters. Both Bergh and Tijdeman [10] and Whitmore [12] seem to indicate that the model parameters are not far from the real values. Nevertheless, a conclusive statement on the usefulness of the MAP parameters when used with corrective models remains to be analyzed in further research.

Finally, the semi-empirical calibration method may be useful in other interesting scenarios. One such case is the in-situ calibration of microphone probes installed on non-sealing surfaces. Many multi-step calibration approaches require that the internal pressure field within the calibrator does not vary by more than an amplification constant, as explained in Section 1. Yet, when the microphone probe is mounted on a surface with which the calibrator cannot form a seal, e.g., on porous or strongly curved surfaces [52], no

controlled calibration environment can be created. A single calibration step would remove the requirement of an identical pressure field over multiple steps, but the acquired TF would be defined as the combination of the TF of the probe and that of the calibrator, with no means of separating them from each other. Using ASSIST, the calibration data would be fitted with a W model line-cavity representation of both the calibrator and microphone probe geometries (see the left-most TF in Figure 13). Afterwards, only the line-cavity elements of the microphone probe can be kept, while discarding those associated with the calibrator geometry, resulting in an estimated TF for the microphone probe alone (see the right-most TF in Figure 13).

The concept explained above is exemplified with data from an empirical calibration of a pinhole-mounted microphone, where the set-up, methodology, and microphones are those used for fitting the RMP case in Figure 15 from Moriaux et al. [22]. This empirical dataset also serves as further experimental validation of ASSIST. The TF from the calibrator *side* branch to the pinhole probe onto which the calibrator is placed is used for the fit. Even with the added complexity of 6 fitting parameters, the W model closely matches the empirical data. In the absence of inviscid resonance, the analytic model easily converges to the appropriate model parameters without the need to tune the prior or band-remove spurious resonance. Since the fitting data come from a single calibration step, no spurious resonance is present (see Figure 13), so ASSIST can fit over the entire frequency range and is not required to ignore frequency bands. The two-step empirical calibration of the same pinhole, together with the TF obtained by applying ASSIST directly to those two-step data with the spurious resonance band-passed to refine the fit, is included in Figure 13 as a reference. The single-step result matches the physical cavity resonance of this conventional calibration while omitting the spurious resonance that the two-step data contain, providing a direct comparison against the conventional approach and a favorable validation of the single-step method.

To quantify the agreement, the root-mean-square error (RMSE) between the model TF and the data is computed separately for the amplitude and the phase according to

$$\mathrm{RMSE} = \sqrt{\frac{1}{N}\sum_{i=1}^{N}(d_i - [\boldsymbol{H} \circ m(\boldsymbol{\theta})]_i)^2}, \tag{18}$$

where d_i and $[\boldsymbol{H} \circ m(\boldsymbol{\theta})]_i$ are the data and the model evaluated at the i-th of the N frequency points, and d denotes either $|\mathrm{TF}|$ or $\angle\mathrm{TF}$. The resulting values are reported in Table 2. The optimal fit reduces the amplitude RMSE to the single-step data from 2.65 to 0.35 and the phase RMSE from 1.40 to 0.06 rad relative to the initial guess. More importantly, the probe TF recovered from the single-step calibration agrees with the two-step data almost as closely as the ASSIST fit applied directly to that two-step data, with an amplitude RMSE of 0.130 against 0.119 and an essentially equal phase RMSE of 0.230 against 0.231 rad. The latter fit additionally required band-passing of the spurious resonance to be refined, whereas the single-step result reaches comparable accuracy without such operator intervention.

Table 2. RMSE for the single-step calibration of Figure 13. Top: W model fit to the single-step data, for the initial-guess and optimal parameters. Bottom: the probe TF derived from the single-step fit, and the ASSIST fit to the two-step data, both compared against the two-step empirical calibration.

	|TF|	**∠TF, Rad**
Fit to single-step data, initial guess	2.651	1.400
Fit to single-step data, optimal	0.349	0.060
Single-step probe TF vs. two-step data	0.130	0.230
ASSIST on two-step data vs. two-step data	0.119	0.231

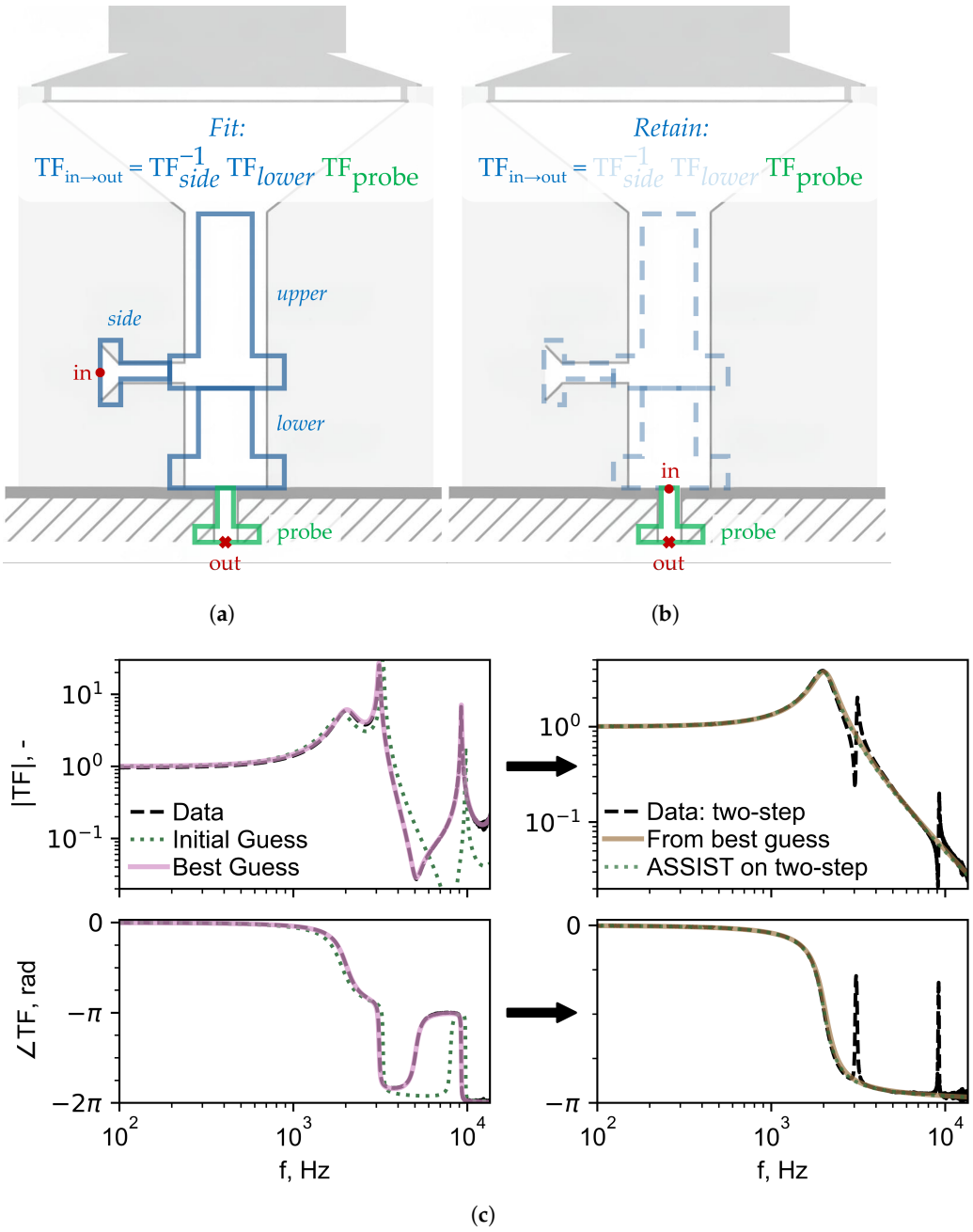


Figure 13. Single-step calibration of empirical pinhole calibration data using ASSIST. Each column shows a step of the approach, including the (**a**,**b**) diagrams of the considered line-cavity elements in the model and (**c**) the TFs. Left: TF fit to the single-step calibration data. Right: W model of the 'empirical dataset' pinhole TF derived from the single-step calibration data fit after removal of the line-cavity elements associated with the calibrator device (dashed-line line-cavity elements). The two-step empirical calibration data of the pinhole, as well as the TF computed by ASSIST based on these data with the spurious resonance band-passed, are included for comparison.

5. Conclusions

The present paper provides the basis for a rigorous and robust single-step calibration of RMPs making use of the novel semi-empirical calibration method ASSIST. Acoustic simulation data have been used as an example dataset to illustrate every step of the method, from its initial setup for a new dataset to the fine-tuning of its parameters for optimal results. The functions of the publicly available repository of the Python code [33] are referenced, enabling readers to set up ASSIST for their calibration data using the provided code.

ASSIST relies on having enough accurate TF data to fit the model, such that the frequency bands affected by spurious resonance are ignored in the fit and replaced by a physically correct TF. Therefore, careful attention should first be paid to acquiring accurate calibration data. Part of the provided Python package aims to process and visualize these data to help the user discern their accuracy during the calibration procedure. Another consequence is that spurious resonance may be included in the TF fit in cases similar to the inviscid resonance presented in this paper or other such edge cases, e.g., the B&K pinhole case in a previous investigation of ASSIST [22]. In these instances, the model parameters are pushed to improbable values. This issue can be solved by (i) restricting the achievable parameter values with the prior or (ii) band-removing the problematic spurious resonance from the data before fitting. Resonance should only be removed after carefully analyzing its origin to ensure that no resonance physical to the microphone probe is erroneously removed.

The subsequent steps for ASSIST are the discretization of the probe geometry into line-cavity elements of the analytic TF model and the definition of the aforementioned prior. Next, the proposal distribution of the MCMC needs to be fine-tuned to achieve a good balance between the acceptance of samples and a low correlation between them. Samples that are too highly correlated may result in an inaccurate estimate of the posterior PDF and, thus, an inaccurate estimate of the uncertainty of the TF fit. The results of each MCMC run aid the user in fine-tuning the parameters of the prior, measurement error variance, and proposal distribution to get closer to the desired TF fit and AR. Hence, ASSIST often requires several MCMC runs to achieve the desired results.

When applying ASSIST to the acoustic simulation dataset of the reference test case, all spurious resonances are correctly removed and replaced. For this particular dataset, the model parameters to which ASSIST converges are sensitive to the chosen prior and differ from the simulation geometry. The source of this discrepancy is that the simulation data consider an inviscid model for the propagation of acoustic waves, whereas the chosen analytic TF model [12] intrinsically considers viscosity. To emulate an inviscid TF with the viscous model, any shear wave number fitting parameter is perpetually pushed to larger absolute values. The correlation between the shear wave number and the other model parameters implies that the other parameters are also affected by the unrealistic value for the shear wave number. Both aforementioned solutions solve the lack of convergence of the fitting parameters, i.e., adapting the prior accordingly or band-removing the inviscid resonance. However, band-removing the inviscid resonance has the additional benefit of decreasing the sensitivity of the found fitting parameter values to the prior.

An important aspect of the proposed methodology is that the model parameters found with ASSIST can be used in correction terms for either TFs or unsteady-pressure measurements to further increase their accuracy. For instance, the estimated radius of the inlet orifice of the probe can be used in the model of Corcos [5] to correct for spatial averaging of unsteady-pressure fluctuations over the sensing area of the probe, or, following Samuelson [53], in a line-cavity model evaluated at the measurement temperature to transfer a calibration to different temperature conditions. In contrast to the inviscid dataset, the model parameters determined by ASSIST are expected to better represent their real-life counterparts for viscous calibration data, making this a potentially feasible future development.

Finally, ASSIST has been shown to be capable of providing an estimated TF for RMPs mounted on a flat sealing surface using a single-step calibration method. This approach eliminates the need to keep the pressure fluctuations within the calibrator identical up to an amplification constant over both calibration steps. For the empirical pinhole case, the probe TF recovered from a single calibration step reproduces the conventional two-

step calibration almost as accurately as ASSIST applied directly to the two-step data, yet without the band-passing of spurious resonance that the latter requires. For microphone probes installed on non-sealing surfaces, such as porous liners [31], this enables their in-situ calibration, which is typically not feasible with current calibration techniques.

Author Contributions: Conceptualization, R.Z.; methodology, R.Z. and O.M.; software, O.M.; validation, O.M.; formal analysis, O.M.; investigation, O.M.; resources, R.Z.; data curation, O.M.; writing—original draft preparation, R.Z. and O.M.; writing—review and editing, R.Z.; visualization, O.M.; supervision, R.Z.; project administration, R.Z.; funding acquisition, R.Z. All authors have read and agreed to the published version of the manuscript.

Funding: This research received no external funding.

Data Availability Statement: The FEM simulation data of the plane-wave tube calibrator and the experimental calibration data of the pinhole-mounted microphone probe used in the article are available in the public repository [33], which also contains the code to process these data.

Acknowledgments: The FEM simulation of the plane-wave tube calibrator has been performed by Christophe Schram.

Conflicts of Interest: The authors declare no conflicts of interest.

References

1. Tijdeman, H. Investigation of the Transonic Flow Around Oscillating Airfoils. Ph.D. Thesis, Delft Technological University, Delft, The Netherlands, 1977.
2. Choudhry, A.; Arjomandi, M.; Kelso, R. A study of long separation bubble on thick airfoils and its consequent effects. *Int. J. Heat Fluid Flow* **2015**, *52*, 84–96. [CrossRef]
3. Stark, R.H.; Genin, C. Scaling Effects on Side Load Generation in Subscale Rocket Nozzles. In Proceedings of the 52nd AIAA/SAE/ASEE Joint Propulsion Conference, Salt Lake City, UT, USA, 25–27 July 2016; pp. 1–14. [CrossRef]
4. Zamponi, R.; Satcunanathan, S.; Moreau, S.; Meinke, M.; Schröder, W.; Schram, C. Effect of porosity on Curle's dipolar sources on an aerofoil in turbulent flow. *J. Sound Vib.* **2023**, *542*, 117353. [CrossRef]
5. Corcos, G.M. Resolution of Pressure in Turbulence. *J. Acoust. Soc. Am.* **1963**, *35*, 192–199. [CrossRef]
6. Hu, N. Sensor-size-related attenuation correction of wall pressure spectra measurements. *Phys. Fluids* **2022**, *34*, 067119. [CrossRef]
7. dos Santos, F.L.; Botero-Bolívar, L.; Venner, C.H.; de Santana, L.D. Analysis of the remote microphone probe technique for the determination of turbulence quantities. *Appl. Acoust.* **2023**, *208*, 109387. [CrossRef]
8. Taback, I. *The Response of Pressure Measuring Systems to Oscillating Pressures*; Technical Report NACA-TN-1819; NACA, Langley Aeronautical Laboratory, Langley Air Force Base: Hampton, VA, USA, 1949. Available online: https://digital.library.unt.edu/ark:/67531/metadc55128/ (accessed on 1 May 2026).
9. Iberall, A.S. Attenuation of Oscillatory Pressures in Instrument Lines. *Trans. Am. Soc. Mech. Eng.* **1950**, *72*, 689–695. [CrossRef]
10. Bergh, H.; Tijdeman, H. *Theoretical and Experimental Results for the Dynamic Response of Pressure Measuring Systems*; National Aerospace Laboratory NLR: Amsterdam, The Netherlands, 1965. Available online: http://resolver.tudelft.nl/uuid:e88af84e-120f-4c27-8123-3225c2acd4ad (accessed on 1 May 2026).
11. Pierce, A.D. *Acoustics: An Introduction to Its Physical Principles and Applications*, 3rd ed.; Springer: Cham, Switzerland, 2019. [CrossRef]
12. Whitmore, S.A. Frequency response model for branched pneumatic sensing systems. *J. Aircr.* **2006**, *43*, 1845–1853. [CrossRef]
13. Whitmore, S.A.; Fox, B. Improved accuracy, second-order response model for pressure sensing systems. *J. Aircr.* **2009**, *46*, 491–500. [CrossRef]
14. Zawodny, N.S.; Liu, F.; Cattafesta, L. Transfer matrix modeling of a recessed microphone for unsteady surface pressure measurements. *Appl. Acoust.* **2017**, *117*, 185–190. [CrossRef]
15. Bynum, D.S.; Ledford, R.L.; Smotherman, W.E. *Wind Tunnel Pressure Measuring Techniques*; Technical Report AGARD-AG-145; North Atlantic Treaty Organization, Advisory Group for Aeronautical Research and Development: Neuilly-sur-Seine, France, 1970.
16. Van de Wyer, N.; Zapata, A.; Nogueira, D.; Schram, C. Development of a test rig for the measurement of turbulent boundary layer wall pressure statistics. In Proceedings of the 2018 AIAA/CEAS Aeroacoustics Conference, Atlanta, GA, USA, 25–29 June 2018. [CrossRef]
17. Englund, D.R.; Richards, W.B. The infinite line pressure probe. *ISA Trans.* **1985**, *24*, 11–19.

18. Awasthi, M.; Rowlands, J.; Moreau, D.J.; Doolan, C.J. Two-step hybrid calibration of remote microphones. *J. Acoust. Soc. Am.* **2018**, *144*, EL477–EL483. [CrossRef] [PubMed]
19. Pérennès, S. Aerodynamic Noise Sources Characterization at Low Frequencies of High-Lift Devices. Ph.D. Thesis, École Centrale de Lyon, Écully, France, 1999. Available online: http://www.theses.fr/1999ECDL0032 (accessed on 1 May 2026).
20. Druault, P.; Hekmati, A.; Ricot, D. Discrimination of acoustic and turbulent components from aeroacoustic wall pressure field. *J. Sound Vib.* **2013**, *332*, 7257–7278. [CrossRef]
21. Debert, S.; Pachebat, M.; Valeau, V.; Gervais, Y. Ensemble-Empirical-Mode-Decomposition method for instantaneous spatial-multi-scale decomposition of wall-pressure fluctuations under a turbulent flow. *Exp. Fluids* **2011**, *50*, 339–350. [CrossRef]
22. Moriaux, O.; Zamponi, R.; Schram, C. Semi-empirical calibration of remote microphone probes using Bayesian inference. *J. Sound Vib.* **2023**, *573*, 118197. [CrossRef]
23. Tijdeman, H.; Bergh, H. *The Influence of the Main Flow on the Transfer Function of Tube-Transducer Systems Used for Unsteady Pressure Measurements*; National Aerospace Laboratory NLR: Amsterdam, The Netherlands, 1972. Available online: http://resolver.tudelft.nl/uuid:3d3e7e72-7949-4d1a-8043-3194c42edff5 (accessed on 1 May 2026).
24. Skilling, J. Classic Maximum Entropy. In *Maximum Entropy and Bayesian Methods*; Springer: Cambridge, UK; Dordrecht, The Netherlands, 1988; pp. 45–52. [CrossRef]
25. Pereira, A.; Antoni, J.; Leclère, Q. Empirical Bayesian regularization of the inverse acoustic problem. *Appl. Acoust.* **2015**, *97*, 11–29. [CrossRef]
26. Azijli, I.; Sciacchitano, A.; Ragni, D.; Palha, A.; Dwight, R.P. A posteriori uncertainty quantification of PIV-based pressure data. *Exp. Fluids* **2016**, *57*, 72. [CrossRef]
27. Schmid, J.M.; Schmid, J.D.; Eser, M.; Marburg, S. *In situ* estimation of the acoustic surface impedance using simulation-based inference. *J. Acoust. Soc. Am.* **2026**, *159*, 422–436. [CrossRef] [PubMed]
28. Wulbusch, N.; Roden, R.; Blau, M.; Chernov, A. Bayesian Parameter Identification in Impedance Boundary Conditions for Helmholtz Problems. *SIAM J. Sci. Comput.* **2024**, *46*, B422–B447. [CrossRef]
29. Dinsenmeyer, A.; Leclère, Q.; Antoni, J.; Julliard, E. A Bayesian approach for the separation of the acoustic and the correlated aerodynamic wall pressure fluctuations. *J. Acoust. Soc. Am.* **2021**, *149*, 4410–4421. [CrossRef] [PubMed]
30. Moriaux, O.K.; Zamponi, R.; Schram, C.F. Development of a Model-Driven Calibration Method for Remote Microphone Probes Using Bayesian Inference. In Proceedings of the AIAA AVIATION 2023 Forum, San Diego, CA, USA, 12–16 June 2023. [CrossRef]
31. Moriaux, O.K.; Zamponi, R.; Satcunanathan, S.; Meinke, M.; Schröder, W. Experimental and Numerical Investigation of the Turbulent Boundary Layer of a Grazing Flow over Porous Materials. In Proceedings of the 30th AIAA/CEAS Aeroacoustics Conference (2024), Rome, Italy, 4–7 June 2024. [CrossRef]
32. Python Software Foundation. *Python Language Reference*, version 3.9.12; Python Software Foundation: Beaverton, OR, USA, 2022. Available online: https://www.python.org (accessed on 8 June 2026).
33. Moriaux, O. Semi-Empirical Calibration Using Bayesian Inference (Version 1.3). 2024. Available online: https://github.com/OMoriaux/SemiEmpiricalCalibrationBayesian (accessed on 8 June 2026).
34. Zingale, N.B.; Zamponi, R.; Christophe, J.; Bricteux, L.; Schram, C.F. Machine-Learning Based Modeling of the Wall Pressure Statistics Part 1: New Experimental Methodology for the Population of Extended Training Databases. In Proceedings of the 32nd AIAA/CEAS Aeroacoustics Conference (2026), Brussels, Belgium, 26–29 May 2026. [CrossRef]
35. Gumley, S.J. A detailed design method for pneumatic tubing systems. *J. Wind Eng. Ind. Aerodyn.* **1983**, *13*, 441–452. [CrossRef]
36. Tijdeman, H. On the propagation of sound waves in cylindrical tubes. *J. Sound Vib.* **1975**, *39*, 1–33. [CrossRef]
37. Sivia, D.; Skilling, J. *Data Analysis: A Bayesian Tutorial*; Oxford Science Publications; Oxford University Press: Oxford, UK, 2006.
38. Dekking, F.M.; Kraaikamp, C.; Lopuhaä, H.P.; Meester, L.E. Conditional probability and independence. In *A Modern Introduction to Probability and Statistics: Understanding Why and How*; Springer: London, UK, 2005; pp. 25–40. [CrossRef]
39. Gelman, A.; Carlin, J.B.; Stern, H.S.; Dunson, D.B.; Vehtari, A.; Rubin, D.B. *Bayesian Data Analysis*, 3rd ed.; Chapman and Hall/CRC: New York, NY, USA, 2013. [CrossRef]
40. Haario, H.; Laine, M.; Mira, A.; Saksman, E. DRAM: Efficient adaptive MCMC. *Stat. Comput.* **2006**, *16*, 339–354. [CrossRef]
41. Shahmoradi, A.; Bagheri, F.; Osborne, J.A. Fast fully-reproducible serial/parallel Monte Carlo and MCMC simulations and visualizations via ParaMonte::Python library. *arXiv* **2020**, arXiv:2010.00724.
42. Project Jupyter. Jupyter. 2024. Available online: https://jupyter.org (accessed on 8 June 2026).
43. Virtanen, P.; Gommers, R.; Oliphant, T.E.; Haberland, M.; Reddy, T.; Cournapeau, D.; Burovski, E.; Peterson, P.; Weckesser, W.; Bright, J.; et al. SciPy 1.0: Fundamental Algorithms for Scientific Computing in Python. *Nat. Methods* **2020**, *17*, 261–272. [CrossRef] [PubMed]
44. Siemens Digital Industries Software. Simcenter. 2023. Available online: https://plm.sw.siemens.com/en-US/simcenter/ (accessed on 8 June 2026).
45. Basten, T.G.H.; de Bree, H.E. Full bandwidth calibration procedure for acoustic probes containing a pressure and particle velocity sensor. *J. Acoust. Soc. Am.* **2010**, *127*, 264–270. [CrossRef] [PubMed]

46. Buck, M.; Cahill, B.; Davis, R.T.; Gander, M.; Hayes, W.; Henricksen, C.A.; Keele, D.; Klepper, D.; Murray, F.M.; Owen, G.; et al. *AES Information Document for Acoustics—Plane-Wave Tubes—Design and Practice*; Technical Report AES-1id-2012; Audio Engineering Society, Inc.: New York, NY, USA, 2017.
47. Henze, N. Kolmogorov–Smirnov Test. In *The Concise Encyclopedia of Statistics*; Springer: New York, NY, USA, 2008; pp. 283–287. [CrossRef]
48. Dwight, R.P.; Buchanan, T.S.B. Uncertainty Quantification: Propagation and Inversion in Complex Models. April 2022. Available online: https://aerodynamics.lr.tudelft.nl/~rdwight/cfdiv/index.html (accessed on 8 June 2026).
49. Tarantola, A. Inverse Problem Theory and Methods for Model Parameter Estimation. In *Inverse Problem Theory and Methods for Model Parameter Estimation*, 1st ed.; Chapter 3.2.2; Society for Industrial and Applied Mathematics: Philadelphia, PA, USA, 2005; pp. 64–68. [CrossRef]
50. van Ravenzwaaij, D.; Cassey, P.; Brown, S.D. A simple introduction to Markov Chain Monte–Carlo sampling. *Psychon. Bull. Rev.* **2018**, *25*, 143–154. [CrossRef] [PubMed]
51. Dekking, F.M.; Kraaikamp, C.; Lopuhaä, H.P.; Meester, L.E. Exploratory data analysis: Graphical summaries. In *A Modern Introduction to Probability and Statistics: Understanding Why and How*; Chapter 15; Springer: London, UK, 2005; pp. 207–230. [CrossRef]
52. Zamponi, R.; Satcunanathan, S.; Moreau, S.; Ragni, D.; Meinke, M.; Schröder, W.; Schram, C. On the role of turbulence distortion on leading-edge noise reduction by means of porosity. *J. Sound Vib.* **2020**, *485*, 115561. [CrossRef]
53. Samuelson, R.D. *Pneumatic Instrumentation Lines and Their Use in Measuring Rocket Nozzle Pressure*; Technical Report RN-DR-0124; Aerojet-General Corp.: Sacramento, CA, USA, 1967.

Disclaimer/Publisher's Note: The statements, opinions and data contained in all publications are solely those of the individual author(s) and contributor(s) and not of MDPI and/or the editor(s). MDPI and/or the editor(s) disclaim responsibility for any injury to people or property resulting from any ideas, methods, instructions or products referred to in the content.